Peridynamic analysis to investigate the influence of microstructure and porosity on fatigue crack propagation in Additively Manufactured Ti6Al4V

Olena Karpenko*, Selda Oterkus, Erkan Oterkus,

Department of Naval Architecture, Ocean and Marine Engineering, University of Strathclyde, 100 Montrose Street, Glasgow G4 0LZ, United Kingdom

*Corresponding author: olena.karpenko@strath.ac.uk

Abstract

Additive Manufacturing (AM) has gained a lot of interest due to the freedom to produce complex metal geometries directly from the designed digital model. Despite the high potential of AM, the process induced imperfections, like pores and the microstructural changes due to the layer-by-layer manufacturing, made a significant impact on the fatigue resistance and crack growth behaviour. Consequently, this work aims to evaluate the effect of microstructure and existence of pores in additively manufactured Ti6Al4V on Fatigue Crack Growth (FCG) utilizing bond-based Peridynamics (PD) fatigue model. Employing the columnar granularity and different levels of porosities indicated a substantial impact on FCG rates.

Keywords: *Peridynamics; Additive manufacturing; microstructure; porosity defects; fatigue performance prediction*

1 Introduction

Additive manufacturing process is a 3D printing technology that has gained a lot of interest in aerospace, civil, automotive and biomedical industries [1–5], as well as marine industry [6,7]. The production process of additively manufactured structures is based on adding thin layers of the material according to the designed digital 3D model [3]. This unique process allows the production of complex or customised geometries directly from the design file utilising commercial software [3] without the necessity of casting moulds or dies. In addition, the material efficiency is higher than the conventional processing methods, and prototyping and rapid fabrication are the significant advantages of AM.

This is a peer-reviewed, accepted author manuscript of the following article: Karpenko, O., Oterkus, S., & Oterkus, E. (2022). Peridynamic analysis to investigate the influence of microstructure and porosity on fatigue crack propagation in additively manufactured Ti6Al4V. Engineering Fracture Mechanics, 261, [108212]. https://doi.org/10.1016/j.engfracmech.2021.108212

Nomenclature

Latin Characters

a	Crack length
a_n	Pre-notch length
A, m	Material constants in the PD fatigue model
A_1, m_1	Material constants for Phase I (crack nucleation) in the PD fatigue model
A_2, m_2	Material constants for Phase II (crack propagation) in the PD fatigue model
b	Peridynamic constant for in-plane deformations
$\boldsymbol{b}$	The vector of body loads
b_y	Body force density
$\boldsymbol{B}$	Body load matrix
d	Diameter of the pins in C(T) sample
d_p	Pore diameter
E	Young's modulus
$\boldsymbol{f}$	Peridynamic pairwise force densities
F_a	Cyclic load amplitude
ΔF	Cyclic load range with cyclic load extremes F_y^{max} and F_y^{min}
h	Thickness of the sample
H_x	Horizon of the material point with coordinates x
k	Grain coefficient with k_{GI} for grain boundaries and k_{GB} for grain interior
$\boldsymbol{K}$	Global stiffness matrix
ΔK	Stress intensity factor
ΔK_p	Stress intensity factor for pores
$\Delta K_{th,p}$	SIF range limit for specified pores
$\Delta K_{th,LC}$	Threshold SIF range for the long crack
L	Length of the sample
M	Total number of the family members
n	Cycle range
N	Number of loading cycles
N_f	Number of cycles to crack nucleation
$N_{p_{tot}}$	Total number of pores
P	Porosity ratio
R	Load ratio
$s_{(i)(j)}$	Stretch between material points i and j
s^{max}, s^{min}	Maximum and minimum bond stretches
t	Time
$\boldsymbol{u}$	Displacement vector
$\ddot{\boldsymbol{u}}_{(i)}$	Acceleration vector of the material point i
$\boldsymbol{U}$	Displacement matrices
V	Incremental volume
ΔV_Δ	Volume of the boundary layer
V_p, V_T	Volume of void-space and a bulk volume of material
W	Width of the sample
$\boldsymbol{x}$	Vector of coordinates
Δx	Spacing between material points
$\boldsymbol{y}$	Location of the material point after deformation

Greek Characters

δ	Horizon size
ε	Cyclic bond strain
η_x, η_y	Relative displacements between material points in x and y directions
λ	Remaining life of the bond

μ	Shear modulus
ν	Poisson's ratio
$\boldsymbol{\xi}$	Relative position vector
ξ_x, ξ_y	Reference lengths in x and y directions
ρ	Mass density
σ_a	Stress amplitude
$\sigma_y^{max}, \sigma_y^{min}$	Maximum and the minimum stresses
$\Delta\sigma_e$	Intrinsic fatigue limit
φ	Local damage of each material point
χ	Pore coefficient
ψ	State of the bond (intact or broken)
Abbreviations	
ADR	Adaptive dynamic relaxation
AM	Additive manufacturing
C(T)	Compact tension sample
EBM	Electron beam melting
FCG	Fatigue crack growth
FCGR	Fatigue crack growth rates
H-C(T)	Horizontal compact tension sample
PD	Peridynamics
SIF	Stress intensity factor
SLM	Selective laser melting
V-C(T)	Vertical compact tension sample
VHCF	Very high cycle fatigue
WAAM	Wire+arc additive manufacturing

Metal AM is the newer field of AM technology, developed over the past 20 years, becoming a state-of-the-art manufacturing process of complex structural shapes [4,8]. Titanium, aluminium, stainless steel and nickel superalloys are the most commonly used alloys in AM [9,10]. Each material has its applicability in different fields because of its mechanical properties, production challenges and costs. Titanium alloys Ti6Al4V are among the most attractive materials due to their outstanding combination of high specific strength, low density and corrosion resistance [11], with the only drawback of its high cost of fabrication. Multiple studies are undergoing on AM of Ti6Al4V to reduce the manufacturing cost and widen its industrial applications. The studies' focus is on different Ti6Al4V AM process techniques, resulting in a good quality AM of fabricated metal with properties close to the standard cast and wrought product. Some of the most common methods used for Ti6Al4V AM processes can be distinguished by the type of material used, like wires for the wire+ arc AM (WAAM) and the metallic powders for Selective Laser Melting (SLM) or Electron Beam Melting (EBM). All the AM processes require the designed 3D computer model, the processing steps, and the post-processing. The computer-aided design (CAD) file is used for 3D part fabrication and the appropriate sensors are controlling the processing conditions. After the deposition process is over, the fabricated part requires post-processing operations, like chemical polishing, machining grinning and peening. The carefully controlled processing conditions such as a feed rate of the feedstock material, speed of the heat source and finishing operations can result in a desired product outcome [12,13].

AM showed a great potential of titanium alloys manufacturing because of geometrical flexibility, reputability, surface quality and productivity [9]. However, an essential drawback of layer-by-layer manufacturing is the anisotropy of the material properties of the additively manufactured components [14]. The rapid and repeated heating and cooling of the AM process leads to variations in the microstructure, the properties (layer quality) and internal stresses in different regions [15,16]. Another negative outcome of the AM is the occurrence of pores due to the powder [17] or wire [18] contaminations, vaporisation when the temperatures in the molten pool are very high [19], leading to the entrapped gases or vapours in the material [9]. Eventually, microstructure with pores that act as a strong stress raiser and residual stresses impact the structure's performance under different loading conditions [20], especially fatigue loading.

The studies on FCG in additively manufactured titanium alloys [14,21,22] indicated a strong impact of grain shape and size on FCG performance. There has been an increasing amount of literature [23–26] focused on finding the relationship between the AM process parameters and the mechanical properties of the final structures. Processing parameters such as heating and cooling rates, temperature gradients, the heat source, and layer thickness during the AM significantly impact the microstructural characteristics.

The evaluation of the AM microstructure indicated the presence of elongated columnar prior β grains, which are growing parallel to the build direction due to the rapid solidification process [11,16,24,25,27]. The epitaxial growth of grains occurs during the solidification process from the previously deposited layer and is dependent on the temperature gradients and tilts in the laser scanning direction [17,25]. The columnar prior β grains bring anisotropy in the mechanical properties and fatigue properties in different orientations [28]. However, in various AM processes, different morphologies were reported. For example, looking at the WAAM samples [24,27], columnar prior β grains with the thickness of the grains ranging from 1 to 3 mm have been noticed. On the other hand, the implementation of the rolling process in AM showed a reduction of the prior β grains size with decreased size of increasing rolling load. This means that different processing and post-processing techniques can change the material microstructure and as a result its fatigue properties. The damage in SLM Ti6Al4V due to the cycling loading initiates at the grain boundaries α along the prior β grains with the intergranular α fracture mode [29,30]. As the crack propagation mechanism is effected by the microstructure, the annealing process of the SLM structures is decreasing the size of $\alpha - phase$ with increased fatigue performance [21].

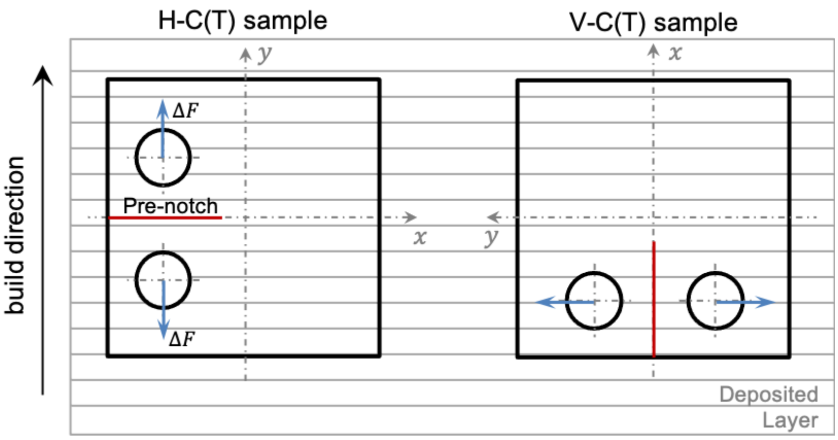

Fig. 1 Horizontal compact tension H-C(T) and vertical compact tension V-C(T) specimen cut.

As reported in the experiments [21] on the Ti6Al4V, produced by SLM, showed lower Fatigue Crack Growth Rates (FCGR) than forged Ti6Al4V, and only after employment of the heat-treated procedure, the FCGR were close to the conventionally processed alloy. Moreover, the test results [21] indicated the variations of the FCG behaviour in the horizontal compact tension (H-C(T)) and vertical compact tension (V-C(T)) samples. In the H-C(T) samples, the FCG is perpendicular to the build direction; instead, in V-C(T) samples, the crack is located perpendicular to the deposited layers, as shown in Fig. 1. The tests' outcome indicated that the FCGR of the H-C(T) samples is greater than the ones in the V-C(T) samples. Instead, the experiment [14] on WAAM and EBM [15] titanium alloy samples showed contrary results compared to SLM with the faster FCG in H-C(T) samples. The evaluation of the SLM produced structures indicated that the fine-grained and martensitic microstructure tend to increase crack propagation [31]. The same pattern is noticed for the wrought titanium alloys [22], where the coarse-grained lamellar microstructure has higher FCG resistance. The coarse-grained lamellar microstructures consist of large β grains with an equivalent circle diameter of around 1 mm [22].

Although the columnar grains were observed in the SLM and WAAM systems, the microstructure of samples produced by the powder is finer compared to the wire fed system. The size of the columnar β grains could bring differences in the FCGR of SLM and WAAM samples, as the fatigue tests of SLM C(T) sample indicated the intergranular propagation in both H-C(T) and V-C(T) samples [32]. The samples built with EBM process showed the FCG through the prior β grains in the H-C(T) sample and along in V-C(T) samples [15].

Another substantial effect is the additively manufactured process-induced defects. The tests' results [21,25,33–35] showed that the stress concentrations at the defects significantly reduce the fatigue strength, and the pores' presence leads to crack initiation at the pore location. Voids and porosities are common defects in AM, as the in-situ X-ray computed tomography scanning on Ti6Al4V samples indicated the porosity volumes of 0.01-0.04% for WAAM [36], 0.08-0.2% [37] and even higher [17] for SLM. Firstly, the existence of pores is observed in the regions of non-melted powder for SLM [17] and the manufacturing with a contaminated wire during WAAM [18]. Secondly, the high power densities and high melting temperatures can lead to entrapped vapours or gases in the melting pool, resulting in microscopic spherical shape pores [9,19]. Moreover, the heat input should be carefully controlled as very high scanning speeds decrease the pool size and decrease the previous layer's penetration depth with the outcome of the lack of fusion porosity formation [24]. In general, the lack of fusion defects could be the most critical defect in the sample due to the size larger than gas pores and the non-symmetrical shape with sharp edges resulting in high-stress concentrations.

The presence of pores in the material directly impacts the fatigue properties, and reducing the porosity in the samples is one of the most important AM processes to increase the fatigue life. The studies [21,25,33] showed that the fatigue properties have much scattered in the experimental data due to the presence of pores in different locations of the samples where the fatigue crack nucleation starts at the pore location. The internal defects showed a critical impact on the fatigue life of the additively manufactured components. The defect size, location, volume of fraction and morphology plays an important role in fatigue performance. It was found that the additively manufactured samples have a shorter fatigue life compared to the wrought Ti6Al4V samples because of the effect of internal defects located near the surface [24,25]. The samples with the largest pores and the areas with a more significant porosity had the shortest fatigue life [33]. The sizes and locations of the pores have a great dependency on the AM process parameters, where the dimensions of pores can vary and can be even larger than $400\mu m$ [15].

Significant efforts were made to study the effect of post-processing techniques, like heat treatments and Hot Isostatic Pressing (HIP), in order to improve the fatigue performance of AM samples. Leuders et al. [21] showed that heat treatments and HIP coarsen the microstructure and release the residual stresses of the samples, but HIP also closes the internal pores. Different HIP and heat treatments improved the fatigue performances, but closing the pores has secondary importance on the fatigue performance compared to the changes in microstructure and decrease in residual stresses.

Evaluation of the additively manufactured sample fatigue performance in the literature brought a lot of discussion on the crack initiation sites at the pores due to its drastic impact on the fatigue life, but the crack propagation profiles are more referred to the sample microstructure. Some test studies [21] indicated that pores did not have a significant impact on the FCG of the samples with pores of the diameter of $d_p \leq 50\mu m$. On the other hand, a review of fatigue performance of additively manufactured Ti6Al4V samples [38] mentioned the contribution of both the microstructure and the process-induced defects.

In this respect, it is essential to evaluate the impact of microstructure and porosities on the FCG performance of additively manufactured Ti6Al4V. The current study aims to predict the fatigue fracture in C(T) samples and analyse the contribution of different types of microstructures and different levels of porosities on FCG by using PD [39]. PD has been successfully applied to fatigue problems to predict crack nucleation and propagation [40–42] and the influence of the porosity on the fatigue life of the metal samples [43]. Authors in [43] proposed a numerical approach to implementing the pores in the PD fatigue model. They showed good predictability of fatigue life of dog-bone samples under high cycle fatigue. In this respect, the authors extend the proposed approach to FCG problems and analyse the effect of the additively manufactured columnar microstructure and process-induced defects in the structures on the FCG.

The paper is organised as follows, where Section 2 presents an overview of the PD model for brittle damage and extension for the fatigue damage and the numerical fatigue model set up for the C(T) sample of wrought titanium alloy. Section 3 reviews the previous studies regarding the microstructure of AM and its effect on FCG. The variations of FCG due to different grain shapes and sizes because of the layer-by-layer process are numerically analysed by PD. In addition, the effect of porosities on the FCG is discussed by the numerical implementation of porosities and analysis in Section 4. Finally, the fatigue performance is analysed for the model with columnar granularity and sample porosities. The conclusions are given in Section 5.

2 Methodology

2.1 Peridynamic model for brittle damage

The bond-based PD introduced by Silling [39] is a reformulation of the fundamental equations of continuum mechanics, which are particularly suitable to solve problems including discontinuities. In addition, PD uses integro-differential equations instead of partial differential equations as in classical continuum mechanics. This widens the possibility of solving fracture mechanics problems, including cracks initiation and propagation [44].

The PD equation of motion can be written in the form of the integro-differential equation as [45]:

$$\rho(\boldsymbol{x})\ddot{\boldsymbol{u}}(\boldsymbol{x},t) = \int_{H_x} \boldsymbol{f}(\boldsymbol{u}(\boldsymbol{x}',t) - \boldsymbol{u}(\boldsymbol{x},t), \boldsymbol{x}' - \boldsymbol{x})dV_{x'} + \boldsymbol{b}(\boldsymbol{x},t) \tag{1}$$

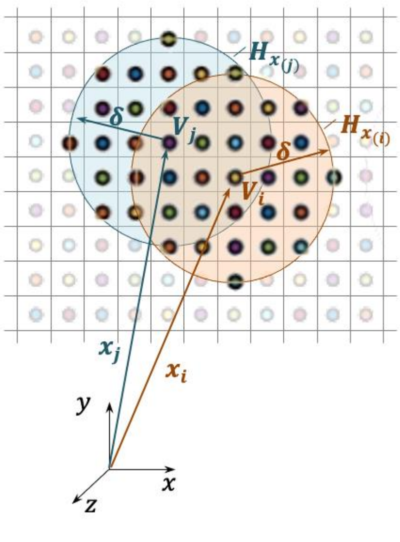

Fig. 2 PD material points and interaction of material points *i* and *j*.

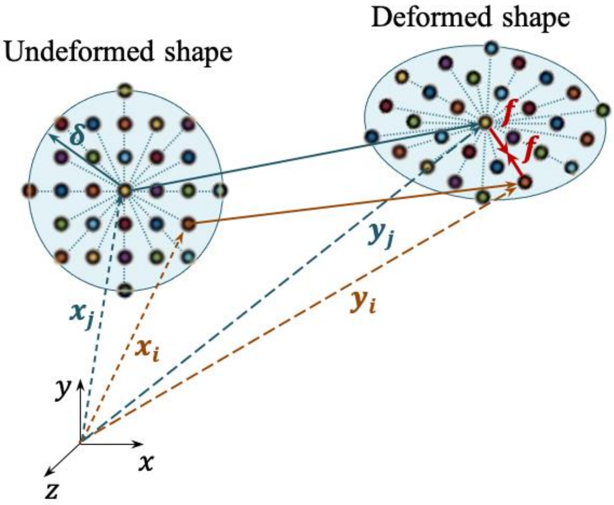

Fig. 3 PD material points *i* and *j* in the deformed configuration and the PD forces between these material points.

which can be discretised as [45]

$$\rho_{(i)}\ddot{\boldsymbol{u}}_{(i)} = \sum_{j=1}^{M} \boldsymbol{f}_{(i)(j)}V_{(j)} + \boldsymbol{b}_{(i)} \tag{2}$$

from which the acceleration $\ddot{\boldsymbol{u}}_{(i)}$ of the material point i at a time t can be obtained. Each material point i interacts with other material points j within its horizon H_x with a total number M of the family members for point i, as shown in Fig. 2. The coordinates of a material point are represented as $\boldsymbol{x}$ with the incremental volume V. $\boldsymbol{u}$, $\boldsymbol{b}$ and ρ denote displacement vector field, body load and mass density of the material point, respectively.

In bond-based PD, interacting material points can exert forces on each other with equal magnitudes [45], and for the interacting material points *i* and *j*, PD pairwise force densities can be defined as [46]:

$$f_{(i)(j)} = 4\delta b s_{(i)(j)} \frac{\boldsymbol{y}_{(j)} - \boldsymbol{y}_{(i)}}{\left|\boldsymbol{y}_{(j)} - \boldsymbol{y}_{(i)}\right|} \tag{3}$$

where δ is the horizon size, b is the PD parameter, and s is the stretch between material points. Once a material point displaces to a new location due to deformation of the structure, its new location is specified as $\boldsymbol{y}$ in the deformed configuration, as shown in Fig. 3.

PD parameter b can be related to the material constant of classical continuum mechanics by equating strain energy density of a material point inside a body subjected to isotropic expansion and simple shear loading conditions calculated from classical continuum mechanics and PD [45]. This study uses a 2-Dimensional (2D) model with plane stress conditions, where the plate is discretised with a single layer of material points in the thickness direction. Due to this, the PD parameter is expressed in terms of shear modulus, μ, thickness, h, and horizon size, δ, for a 2D problem as [45]:

$$b = \frac{6\mu}{\pi h \delta^4} \tag{4}$$

The stretch between material points i and j can be expressed as [45]:

$$s_{(i)(j)} = \frac{\left|\boldsymbol{y}_{(j)} - \boldsymbol{y}_{(i)}\right| - \left|\boldsymbol{x}_{(j)} - \boldsymbol{x}_{(i)}\right|}{\left|\boldsymbol{x}_{(j)} - \boldsymbol{x}_{(i)}\right|} \tag{5}$$

2.2 Peridynamic model for fatigue damage

The first PD fatigue model was proposed in [40], suitable only for the FCG phase. Instead, the formulation in [41] describes the possibilities of dealing with three fatigue stages: crack nucleation, crack growth, and final failure. The authors introduced the damage variable called the "remaining life", which is degrading over the fatigue cycles. Each bond of the material points interactions in the PD model is identified by initial remaining life $\lambda(0) = 1$ and the bond is breaking irreversibly when $\lambda(N) \leq 0$. The irreversible bond breakage for fatigue cracking can be implemented by the failure parameter [47], which includes a history-dependent scalar-valued function ψ to represent broken interactions (bonds) between material points:

$$\psi\left(\boldsymbol{x}_{(j)} - \boldsymbol{x}_{(i)}, N\right) = \begin{cases} 1 & \text{if } \lambda(N) > 0 \text{ for all } 1 < N \\ 0 & \text{otherwise} \end{cases} \tag{6}$$

To monitor the accumulated damage of the bonds over the loading cycles N, the local damage of each material point i is defined as:

$$\varphi\left(\boldsymbol{x}_{(i)}, N\right) = 1 - \frac{\sum_{i=1}^{M} \psi\left(\boldsymbol{x}_{(j)} - \boldsymbol{x}_{(i)}, N\right) V_{(j)}}{\sum_{i=1}^{M} V_{(j)}} \tag{7}$$

The introduced evolution law in [41] for the remaining life of the bond is:

$$\frac{d\lambda(N)}{dN} = -A\varepsilon^{m} \tag{8}$$

where ε is the cyclic bond strain for the sample under two extremes of the loading conditions. The application of each extreme in the model results in maximum and minimum bond stretches between material points, so the bond strain is defined as [41]:

$$\varepsilon = \left|s^{max} - s^{min}\right| = |(1 - R)s^{max}| \tag{9}$$

The material behaviour under two extremes is assumed to be linear, so the cyclic bond strain is expressed in Eq. (9) by maximum stretch s^{max} and load ratio $R = s^{min}/s^{max}$.

The parameters A and m in Eq. (8) are the material constants that can be calibrated using the S-N curve data for the crack initiation phase and with Paris law for FCG [41].

For the crack nucleation phase, the parameters A and m are denoted as A_1 and m_1, and can be calibrated from experimental data. Since the initial remaining life of each bond is $\lambda_1(0) = 1$, integrating Eq. (8) leads to:

$$A_1 \varepsilon^{m_1} N_1 = 1 \tag{10}$$

This means that the crack nucleation occurs at:

$$N_1 = \frac{1}{A_1 \varepsilon^{m_1}} \tag{11}$$

Presenting Eq. (11) on a log-log scale, the A_1 and m_1 can be determined by a linear fit to experimental data presented by strain-life relation in log-log scale [41]. The obtained parameters of A_1 and m_1 are used for static solutions to calculate the fatigue life of the sample at the nucleation phase. The remaining life of the bond is in the phase I (crack nucleation) only until the local damage is $\varphi < 0.4$, otherwise, the fatigue damage is moving from phase I to phase II (FCG). The FCG model can be presented by rewriting the Eq. (8) in the following form [48]:

$$\frac{\lambda_{ij}^{n} - \lambda_{ij}^{n-1}}{N(n) - N(n-1)} = -A_2\left(\varepsilon_{ij}^{n}\right)^{m_2} \tag{12}$$

where the remaining life λ_{ij}^{n} of the bond between the material points i and j at the cycle range n is evaluated. The material constants A_2 and m_2 for phase II can be calibrated using the Paris' Law [41] with the data available from the experiments. Moreover, the material points located in the vicinity of the crack tip, within the horizon, are considered at the phase II of the FCG.

2.3 Direct Peridynamic solver for fatigue damage

Fatigue analysis includes multiple static simulations. Most of the studies on PD static or quasi-static solutions use explicit time integration. Moreover, Eq. (2) is introduced in the dynamic form, and a commonly used technique, as Adaptive Dynamic Relaxation (ADR)[44], is implemented in PD theory to solve static or quasi-static problems. However, using the explicit method, the convergence of the static solution can be time-consuming, as too many time steps are required to reach a stable solution. Therefore, such a method for fatigue analysis can be very costly, and some studies are performed using an implicit solution [42]. In the current work, the direct method is used where PD force function for a 2-D problem is expressed in the matrix form [49]:

$$\begin{Bmatrix} f_x \\ f_y \end{Bmatrix} = \frac{4\delta b}{|\boldsymbol{\xi}|^3} \begin{bmatrix} \xi_x \xi_x & \xi_x \xi_y \\ \xi_y \xi_x & \xi_y \xi_y \end{bmatrix} \begin{Bmatrix} \eta_x \\ \eta_y \end{Bmatrix} \tag{13}$$

where ξ is a relative position between material points, $\boldsymbol{\xi} = \boldsymbol{x}' - \boldsymbol{x}$, η_x and η_y are the relative displacements between material points in x and y directions, $\eta_x = u_x(\boldsymbol{x}', N) - u_x(\boldsymbol{x}, N), \eta_y = u_y(\boldsymbol{x}', N) - u_y(\boldsymbol{x}, N)$ and ξ_x, ξ_y are the reference lengths in x and y directions.

To solve a static problem using the direct method, the acceleration term $\ddot{\boldsymbol{u}}$ is omitted from the equation of motion, and the equation will have the following form:

$$\sum_{j=1}^{N} \boldsymbol{f}_{(i)(j)} V_{(j)} + \boldsymbol{b}_{(i)} = 0 \tag{14}$$

Eq. (13) is a local stiffness for each material point, interacting with other material points. The combination of local stiffness matrices results in the global static PD equation written in the matrix form as:

$$\boldsymbol{KU} = \boldsymbol{B} \tag{15}$$

where $\boldsymbol{K}, \boldsymbol{U}$ and $\boldsymbol{B}$ are the global stiffness matrix, the material points displacements and the body load matrices. Eq. (14) is solved to find the displacements of each material point by taking the inverse stiffness matrix $\boldsymbol{K}^{-1}$. For the models with fine discretisation, the global stiffness matrices can be very massive, and it is time-consuming to calculate the $\boldsymbol{K}^{-1}$. To overcome this issue, the stabilised biconjugate gradients method (BiCG) [50] is used. BiCG improves the capabilities of the PD solver by making it faster and smoother convergence. For all the presented simulations, the BiCG method is used with the convergence tolerance of 10^{-6} and a maximum number of iterations of 5000.

2.4 Validity and PD fatigue model parameters calibration

In the presented studies for fatigue damage prediction in C(T) titanium alloy samples, PD is utilised as a primary numerical tool. MATLAB is used as a main programming and computing platform for developing PD numerical tools. As described in Section 2.2, the PD fatigue model requires PD parameters A_1,m_1, A_2 and m_2 calibration, and the wrought titanium alloy Ti6Al4V [31,51] is selected for this purpose. The wrought Ti6Al4V is identified as a reference model with the following homogeneous material properties: Young's modulus $E = 110\ GPa$ and Poisson's ratio $\nu = 1/3$. Moreover, all simulations are performed under Very High Cycle Fatigue (VHCF) loading with assumptions that no plastic flow occurs.

The PD fatigue model described in Section 2.2 contains crack nucleation and propagation phases. Looking at the PD model, which is discretised with the material points, the points located in the vicinity of the crack tip in the C(T) sample will already be at the propagation stage, whereas the other ones are at the nucleation stage. Firstly, the PD parameters A_1 and m_1 are calibrated from the experimental data [51] in Section 2.4.1. Secondly, in Section 2.4.2, the PD parameters A_2 and m_2 are obtained from the Paris' law data [31], and the FCG curves compared with experimental results.

2.4.1 Setups for crack nucleation PD model

The experimental work [51] is performed for the solid cylindrical specimens of Ti6Al4V under the VHCF loading (ASTM standard E466) with different loading ratios and load amplitudes. A 2D dog-bone plate is used in the PD fatigue crack nucleation simulations to simplify the computational model, as shown in Fig. 4. The PD models are discretised with 6600 material points having a uniform spacing of $\Delta \mathrm{x} = 0.3 \times 10^{-3}$ m and horizon size of $\delta = 3.015\Delta\mathrm{x}$. Following the procedure in [41] of parameters calibration utilising the test data [51], the parameters for the PD fatigue crack nucleation are identified as: $A_1 = 1 \times 10^4$ and $m_1 = 4.42$.

Solving the PD discretised model with identified parameters A_1 and m_1 have resulted in fatigue crack initiation at the midplane of the plate shown in Fig. 5, and the number of cycles N_f to crack nucleation due to different stress amplitudes in Fig. 6. The implementation of calibrated parameters showed that the numerical results are in line with the experimental data [51]. The simulations for Phase I are stopped when the local damage is $\varphi = 0.4$, meaning that the damage of the bonds is still at the nucleation phase, before the FCG phase starts.

The plate is subjected to a VHCF with the load ratio of $R = 0.1$ and the stress amplitudes of $\sigma_a = 373,\ 322\ ,297$ and $244MPa$. A static loading, using the direct method described in Section 2.3, is applied as a body force density at the upper and lower edges of the sample [45]:

$$b_y = \frac{\sigma_y W h}{\Delta V_\Delta} \tag{16}$$

where ΔV_Δ is the volume of the boundary layer, and σ_y is the applied stress, which is defined as:

$$\sigma_y = \begin{cases} \sigma_y^{max} = \dfrac{2\sigma_a}{1-R} \\ \sigma_y^{min} = \sigma_y^{max} R \end{cases} \tag{17}$$

where σ_y^{max} and σ_y^{min} are the maximum and the minimum stresses, respectively.

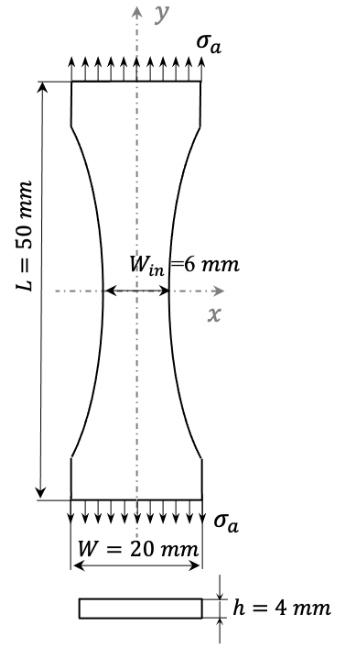

Fig. 4 Geometry of the dog-bone titanium alloy plate.

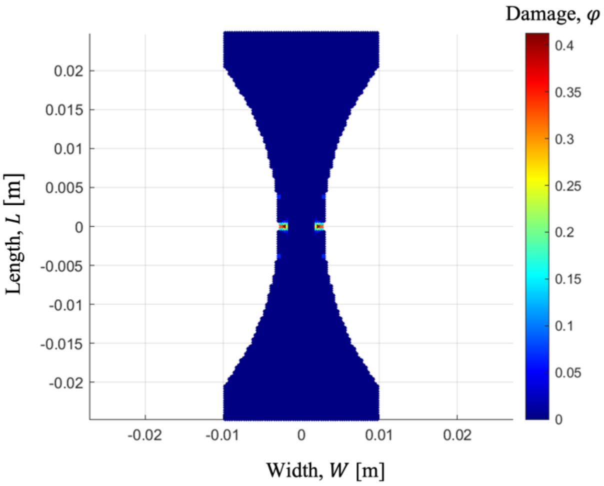

Fig. 5 Damage map for the dog-bone plate under stress amplitude of $\sigma_a = 244\ MPa$ at $N_f = 8 \times 10^7\ cycles$. The damage is identified by local damage $0 < \varphi < 0.4$ in each material point.

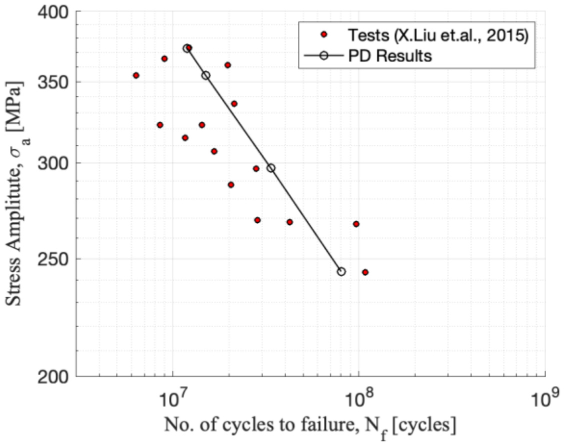

Fig. 6 Stress amplitude as a function of the number of load cycles to failure.

2.4.2 Fatigue crack growth prediction

The PD FCG model is set up for C(T) sample, shown in Fig. 7, with the effective width of $W = 25 \times 10^{-3} m$, thickness of $h = 5 \times 10^{-3} m$ and the pre-notch length of $a_n = 12.4 \times 10^{-3} m$. The crack propagation is analysed for five different cyclic load amplitudes of $F_a = 6.25,\ 5.4,\ 4.5,\ 3.6$ and $3.15\ kN$ with the load ratio of $R = 0.1$. The loads are applied at the pins with the diameter of $d = 6.25 \times 10^{-3}\ m$ as a body force density in the following form:

$$b_y = \frac{F_y}{\Delta V_\Delta} \tag{18}$$

where ΔV_Δ is the volume of the pin area, and F_y is the applied load, which is defined as:

$$F_y = \begin{cases} F_y^{max} = \dfrac{2F_a}{1-R} \\ F_y^{min} = F_y^{max} R \end{cases} \tag{19}$$

where F_y^{max} and F_y^{min} are the cyclic load extremes, respectively.

PD model is discretised with 10400 material points with uniform spacing between them of $\Delta x = 0.3 \times 10^{-3}$ m and horizon size of $\delta = 3.015\Delta x$. Calibrated PD parameters $A_1 = 1 \times 10^4$ and $m_1 = 4.42$ are used for the material points in the crack nucleation phase. PD parameters $A_2 = 0.52 \times 10^6$ and $m_2 = 4.757$ for the FCG phase are obtained from the Paris law data [31]. The FCGR for the mid-region of the crack propagation are evaluated, and the Stress Intensity Factor (SIF) is obtained from ASTM standard E647 [52]:

$$\Delta K = \frac{\Delta F(2+\zeta)}{h\sqrt{W}(1-\zeta)^{\frac{3}{2}}}(0.886 + 4.64\zeta - 13.32\zeta^2 + 14.72\zeta^3 - 5.6\zeta^4) \tag{20}$$

where $\Delta F = F_y^{max} - F_y^{min}$ is a cyclic force range, $\zeta = \frac{a}{W}$, a is the crack length from the location of the applied load as shown in Fig. 7, h is the thickness of the specimen, and W is the distance between the applied load and the edge of the specimen.

The numerical simulations in Fig. 8 are evaluated after the crack propagated around 1mm in order to analyse only the linear region of the $\frac{da}{dN} - \Delta K$ curve, where the fracture toughness can be calculated from Eq. (20), which is applicable when $\zeta > 0.2$ [52]. The FCG curves for five different load cases are compared with the experimental results, where Fig. 9 illustrates the capability of the PD fatigue model to capture the FCG behaviour.

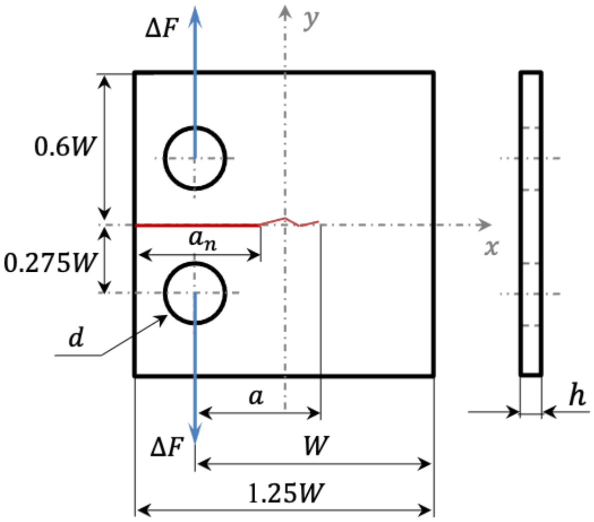

Fig. 7 Titanium alloy C(T) plate under uniaxial tensile loading.

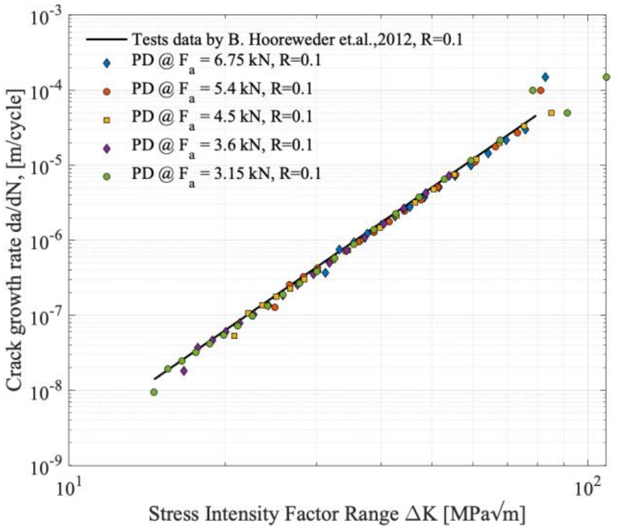

Fig. 8 FCGR versus SIF range.

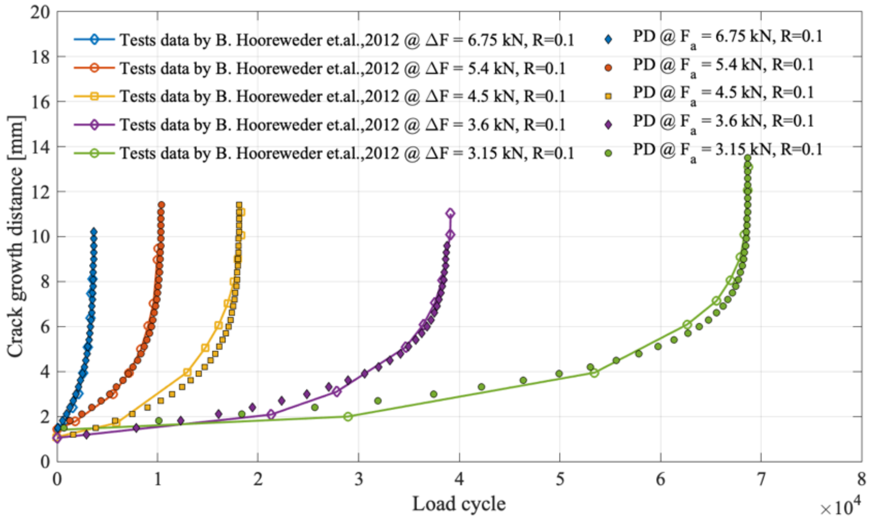

Fig. 9 Crack growth distance versus load cycle for five different load cases.

3 Influence of the microstructure on the FCG

To understand the impact of microstructure on FCG in additively manufactured titanium alloys, different polycrystalline models are generated by the Voronoi tessellation method and are analysed under the constant cycling load amplitudes of $F_a = 3.15kN$ with the load ratio of $R = 0.1$, where the cyclic load extremes are $F_y^{max} = 7kN$ and $F_y^{min} = 0.7kN$. The loads are applied at the pins as shown in Fig. 7 as body force density, evaluated by Eq. (18). The PD FCG model for wrought Ti6Al4V is calibrated and validated with the experimental data in Section 2.4.2 and used to analyse the influence of material microstructure on FCG behaviour due to the AM process. The geometry, shown in Fig. 7, material properties of the C(T) sample and PD parameters are kept the same as stated in Section 2.4.2.

3.1 Modelling of grains in PD

The materials' microstructure is quite a complex phenomenon, which results in divergent fracture behaviour. The experiments reported intergranular and transgranular crack propagation and, additionally, crack deflections. It is essential to understand the cause of the particular behaviour of the crack and the reason for variations in FCGR in the H-C(T) and V-C(T) samples (Fig. 1) produced by AM. Thus, additively manufactured titanium alloys' failure modes are analyzed due to the cycling loading, different types of a polycrystalline model with a variation of the grain and grain boundary strength. The polycrystalline model is generated by the Voronoi tessellation method, where each cell of the Voronoi diagram represents a grain. Therefore, the grains have different grain boundaries (GB) and grain interior (GI) properties. The introduced "interface strength coefficient" [53] for the bonds in a system was used for various fracture problems. PD fatigue model can be expressed as:

$$\begin{cases} \dfrac{\lambda_{ij}^{n} - \lambda_{ij}^{n-1}}{N(n) - N(n-1)} = -kA_1\left(\varepsilon_{ij}^{n}\right)^{m_1}, & \text{for Phase I} \\ \dfrac{\lambda_{ij}^{n} - \lambda_{ij}^{n-1}}{N(n) - N(n-1)} = -kA_2\left(\varepsilon_{ij}^{n}\right)^{m_2}, & \text{for Phase II} \end{cases} \tag{21}$$

where

$$k = \begin{cases} k_{GI}, & \text{for grain interior} \\ k_{GB}, & \text{for grain boundaries} \end{cases} \tag{22}$$

Eq. (21) accounts for two phases of fatigue, including crack initiation (Phase I) and FCG (Phase II), with Eq. (22) for the bonds between material points located inside the same grain and different grains. Fig. 10 visualises points distribution within the plate, where different colours indicate the nodes that belong to a particular grain. Firstly, if the material point is close to the crack with the length of a and in the red region as shown in Fig. 10, then the interactions of the material point with the other ‘family members’ will be at Phase II of fatigue analysis with parameters A_2 and m_2. Secondly, the coefficient k is assigned as k_{GI} for the PD bonds of the material point interacting with the other ‘family members’ which belong to the same grain. Otherwise, coefficient k_{GB} is assigned for the bonds that pass over the grain boundary, as visualised in Fig. 10. As the coefficient k is introduced to the evolution law in Eq. (21), the change in strength of the grain boundaries or grain interior is introduced with the weaker response than the initial structure.

3.2 Effect of the grain size

The experimental studies [14,21,22] showed an impact of grain shape and size on the FCG performance of the titanium alloys. In this section, the effect of the grain size on the fatigue performance of the Ti6Al4V plate is analysed. Based on the observation from the material microstructure, random coordinates are generated to represent the centroids for the Voronoi grains. The selected number of the generated centroids represents the total number of grains in the system. Firstly, the PD polycrystalline models are generated for four configurations with the total number of grains within the sample: a. 500, b. 350, c. 200 and d. 50. Secondly, all four models are simulated under four conditions.

The grain boundaries are weaker than the grain interior, with
C1: $k_{GI} = 1, k_{GB} = 5$
C2: $k_{GI} = 1, k_{GB} = 10$.
The grain interior is weaker than the grain boundaries, with
C3: $k_{GI} = 5, k_{GB} = 1$
C4: $k_{GI} = 10, k_{GB} = 1$.

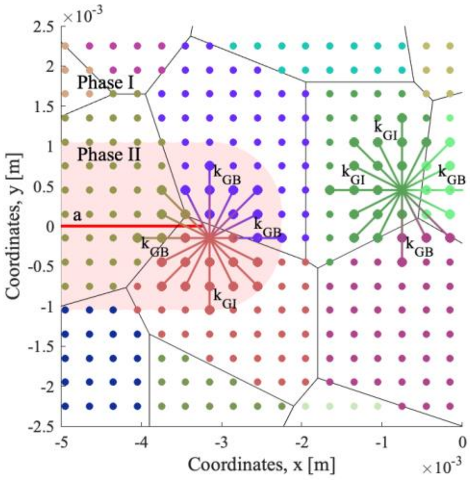

Fig. 10 Interaction between material points and corresponding bond constants.

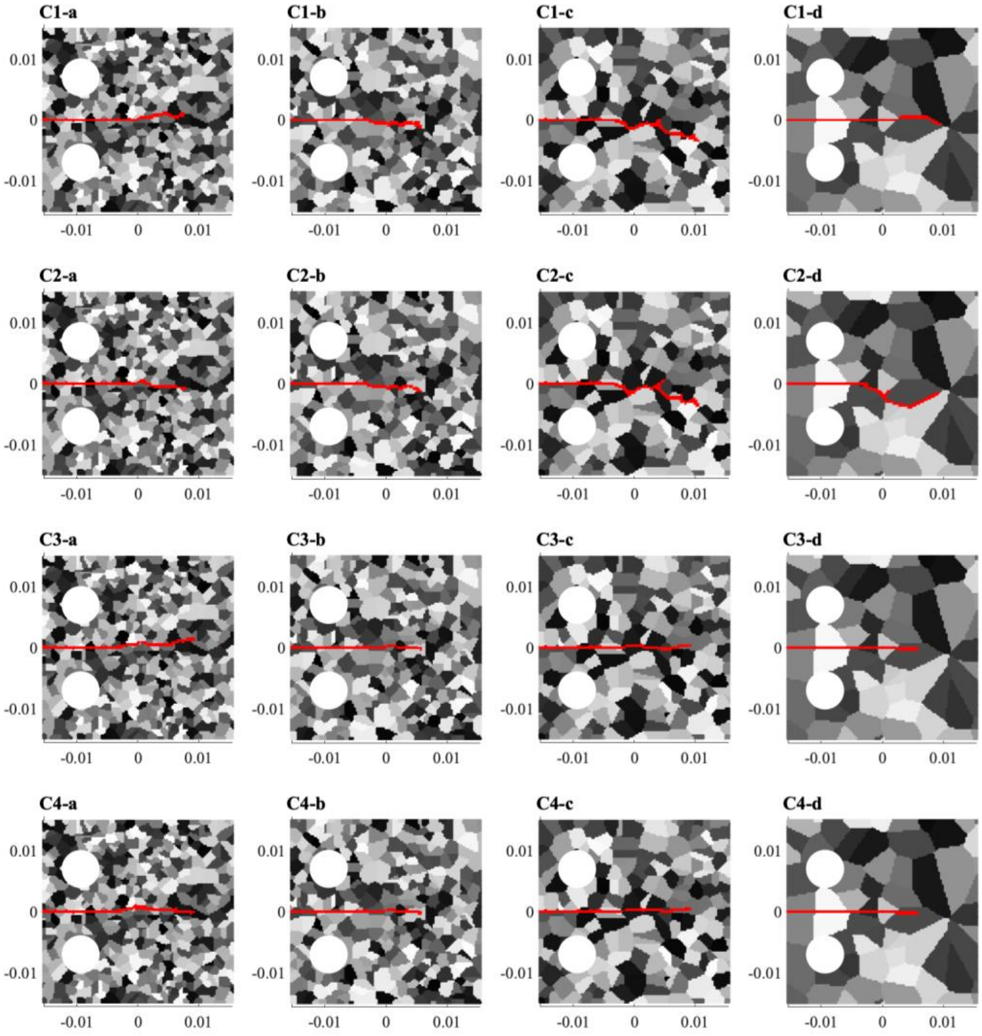

Fig. 11 Damage plots for C(T)-samples under different grain coefficient conditions: C1: $k_{GI} = 1, k_{GB} = 5$, C2: $k_{GI} = 1, k_{GB} = 10$; C3: $k_{GI} = 5, k_{GB} = 1$ and C4: $k_{GI} = 10, k_{GB} = 1$, for the samples with a total number of grains: a. 500, b. 350, c. 200 and d. 50.

The damage maps in Fig. 11 show the intergranular crack propagation for conditions C1 and C2, where the strength of the grain boundaries is lower than the grain interior, and transgranular for C3 and C4, where the strength of the grain boundaries is greater than the grain interior. The intergranular crack propagation can be seen for all grain sizes, which occurs due to the weakness of the bonds crossing the boundaries of the grain. Instead, with a transgranular fracture pattern, the crack propagates through the grain with an almost straight crack path. The grey palette in Fig. 11 indicates the randomly distributed grains, and the crack propagation pattern is displayed in red. The samples with the higher grain coefficients of $k_{GB} = 10$ (C2) or $k_{GI} = 10$ (C4) resulted in a faster crack propagation, as the bonds are weaker compared to the conditions C1 and C3.

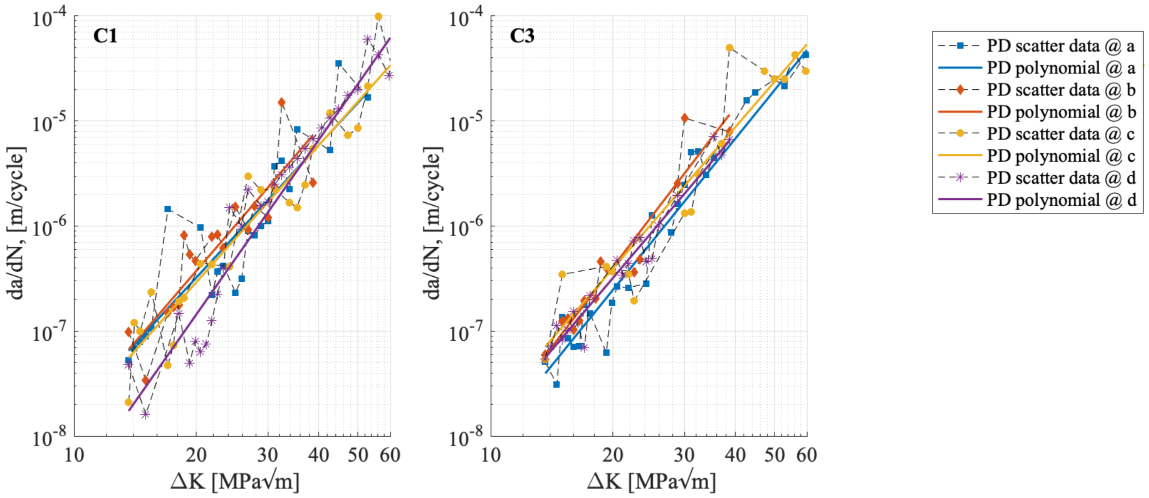

Fig. 12 Crack growth curves for C(T) samples under different grain coefficient conditions: C1: $k_{GI} = 1,\ k_{GB} = 5$ and C3: $k_{GI} = 5, k_{GB} = 1$ and for the samples with a total number of grains: a. 500, b. 350, c. 200 and d. 50.

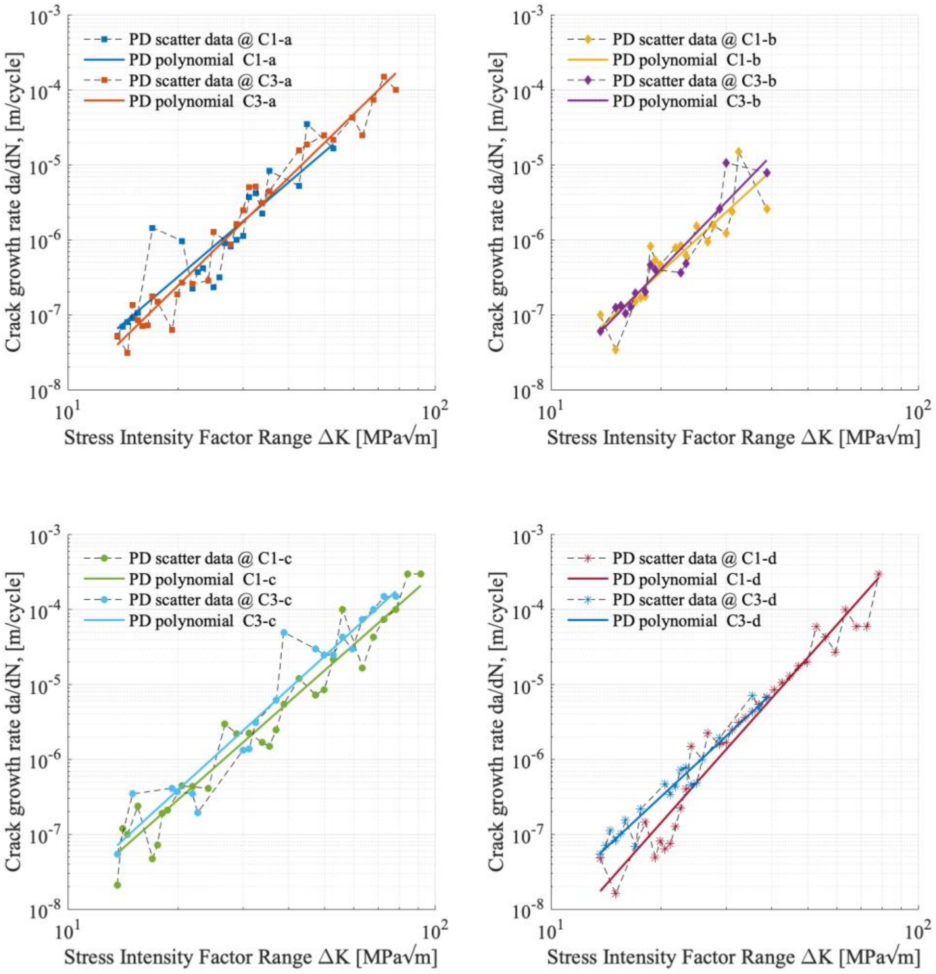

Fig. 13 Crack growth curves comparison for C(T) samples with different granularity: a. 500, b. 350, c. 200 and d. 50 and under different grain coefficient conditions: C1: $k_{GI} = 1, k_{GB} = 5$ and C3: $k_{GI} = 5, k_{GB} = 1$.

The PD results obtained from the FCG samples with condition C1 indicated that the coarser microstructures are more resistant to the FCG. Fig. 12 illustrates that the coarse grain distribution of 50 grains requires a higher number of cycles than the model with a more significant number of grains. The models with fine microstructures (a. 500 grains) have a higher number of weak grain boundaries, which results in a faster FCG. The investigations of the titanium alloy microstructures in [54] concluded that the finer microstructures lead to high FCGR. Hence, the evaluation of the samples under condition C3, where the grain boundaries are stronger than the grain interior, shows a very similar FCG response for all grain models. The crack is suppressed when it reaches the grain boundary and continues propagation through the next grain (Fig. 12, C3).

As the production of the materials can result in different types of microstructures, it is essential to understand the FCG response with intergranular or transgranular crack propagation. Fig. 13 illustrates the comparison of FCGR for the models with different granularity. The numerical results clearly show that the coarser is the model, the better is the response of the samples with an intergranular crack propagation behaviour (sample C1-d). On the other hand, fine granularity models (a. 500 grains) show very close FCGR (Fig. 13) for the samples C1-a and C3-a, even if the crack propagation for C1-a is intergranular and for C3-a is transgranular (Fig. 11).

3.3 Effect of the columnar grains

Due to the layered process of additive manufacturing, the welding layers are annealed several times, which causes the anisotropy of the alloy microstructure. The difference in the grain sizes and elongated structure in the additively manufactured parts brings the anisotropic characteristics and the variations in the fatigue properties in different sample orientations. The microstructure analysis of the produced titanium alloy parts showed the columnar prior- β grains, which are growing parallel to the build direction. To introduce the columnar structure to PD polycrystalline model, the polycrystalline structure is generated by implementing the Voronoi tessellation technique. Similar to another study [55], the random coordinates are generated representing the centroids of the Voronoi grains and after contracted in x- or y-direction. For example, Fig. 14 shows the PD polycrystalline model generation steps, starting from the Voronoi tessellation technique, followed by step 2 of contraction in the x-direction by a factor of 0.1. Finally, the last step is finding the material points within the specified grain boundaries, then identifying the points located within the specified C(T) sample dimensions and assignment of material points associated with the grain. The contraction of the structure in the x-direction presents the H-C(T) sample (Fig. 1), where the columnar grains are allocated perpendicular to the deposited layer and for the representation of the V-C(T) sample structure, the contraction of the grains is in the y-direction. Moreover, the third type of structure is generated with the columnar grain inclination by 45 degrees. For all three types of samples (a. H-C(T), b. V-C(T) and c. 45-C(T)), the grains are generated randomly, and, for the given domain, the number of grains is controlled by the overall of 120 columnar grains per sample with the grain size of around 10 mm in length and 1 mm in width. The numerical study is performed for the samples with assigned C1: $k_{GI} = 1, k_{GB} = 5$; C2: $k_{GI} = 1, k_{GB} = 10$; and C4: $k_{GI} = 10, k_{GB} = 1$.

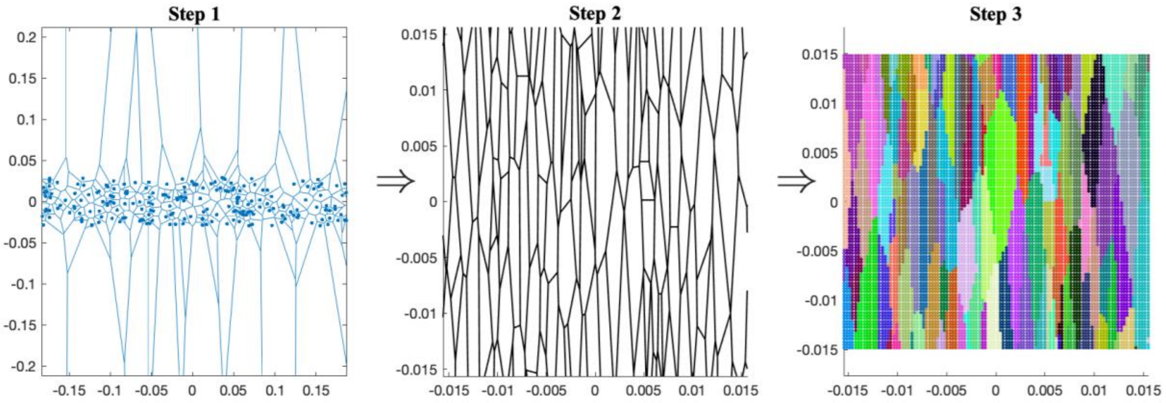

Fig. 14 Generation of columnar grains from Voronoi tessellation technique.

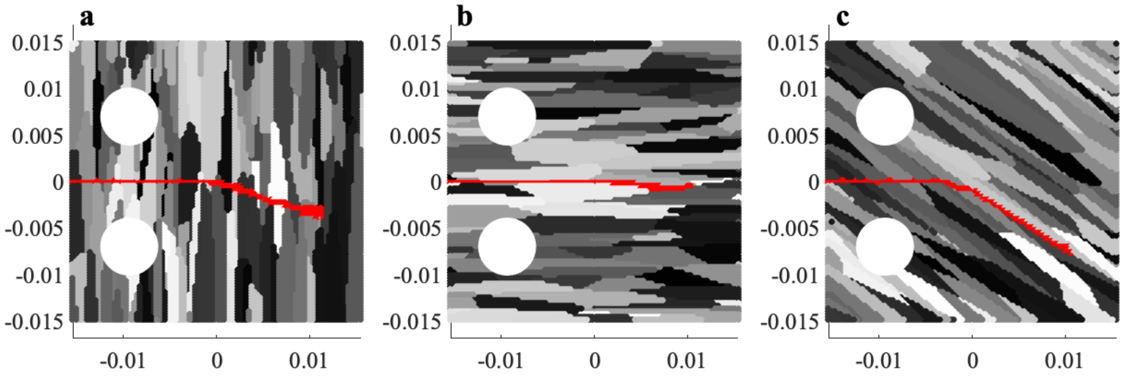

Fig. 15 Damage plots for C(T)-samples under C1 with $k_{GI} = 1, k_{GB} = 5$: **a.** H-C(T), **b.** V-C(T) and **c.** 45-C(T)

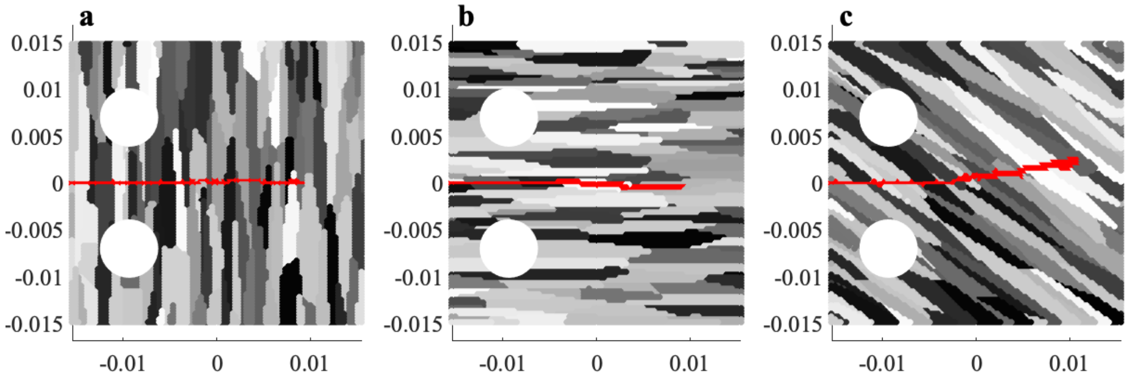

Fig. 16 Damage plots for C(T)-samples under C4 with $k_{GI} = 10, k_{GB} = 1$: **a.** H-C(T), **b.** V-C(T) and **c.** 45-C(T).

The damage maps in Fig. 15 show the transgranular crack propagation in H-C(T) samples, where the crack (indicated in red) passes through the multiple long grains (indicated in the grey scheme). Instead, when the columnar grains are distributed parallel to the initial crack (V-C(T) samples) or with 45 degrees of inclination (45-C(T) samples), the crack propagation is intergranular. Moreover, if the crack tip of the pre-crack is located inside the grain, the crack will move towards the closest grain boundaries and follow the path in-between two long grains. For the model with grains located perpendicular to the pre-crack (Fig. 15a), the crack selects the path with the thinnest grains having the higher number of weak grain boundaries on its way. Furthermore, as the crack repeatedly passes through multiple grains in the H-C(T) sample, this brings some resistance to the crack path, and the crack propagates longer (Fig. 17). The V-C(T) and 45-C(T) samples (Fig. 17, C1) showed very close results of FCGR with the decreased scatter data.

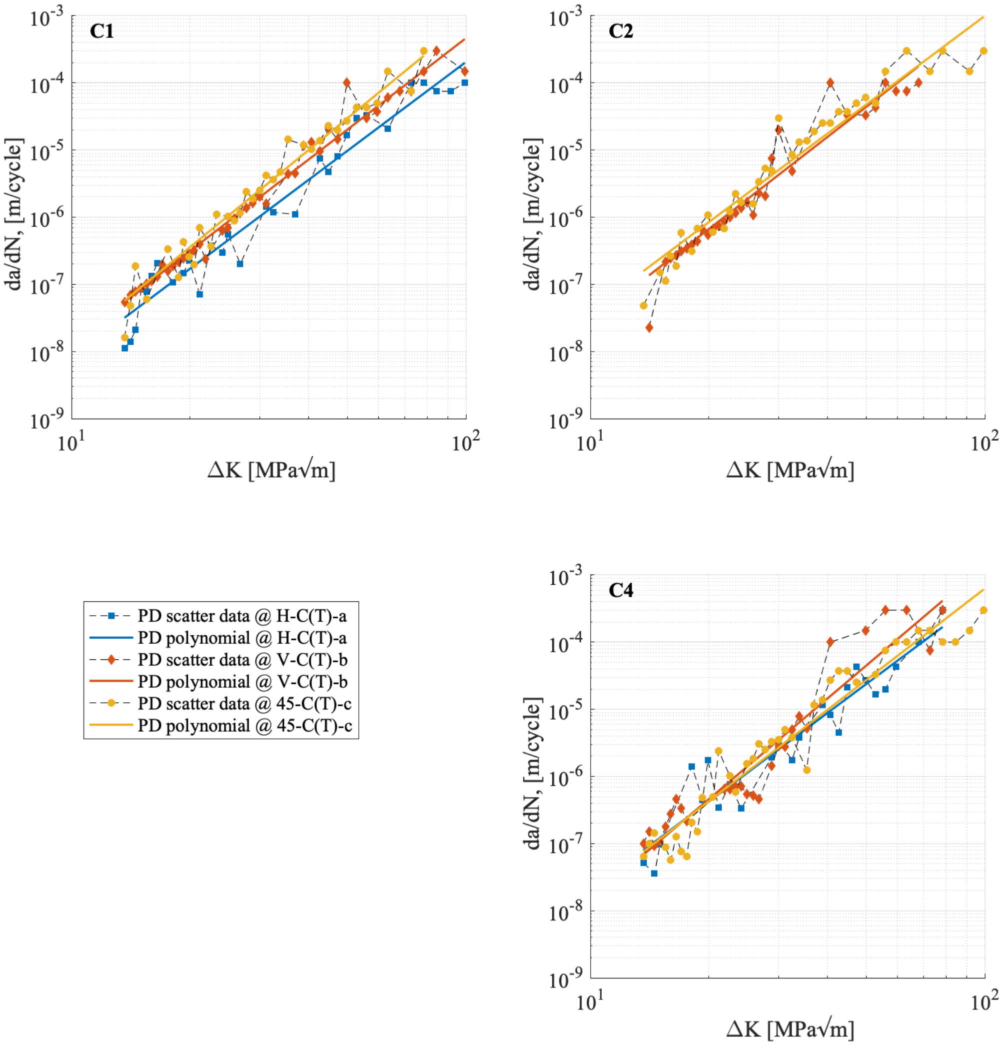

Fig. 17 Crack growth curves comparison for CT samples with different granularity: **a.** H-C(T), **b.** V-C(T) and **c.** 45-C(T), and under different grain coefficient conditions: C1: $k_{GI} = 1, k_{GB} = 5$, C2: $k_{GI} = 1, k_{GB} = 10$ and C4: $k_{GI} = 10, k_{GB} = 1$.

Additionally, the FCGR are evaluated for the models with the grain coefficient $k_{GI} = 1, k_{GB} = 10$ (Fig. 17, C2), where the crack propagation path is similar to the model with $k_{GI} = 1, k_{GB} = 5$ (C1), but the crack is propagating faster. The columnar grain model is simulated for the structures with strong grain boundaries, meaning $k_{GI} = 10, k_{GB} = 1$ (Fig. 17, C4), where the grain direction does not have a significant effect on the crack behaviour with the transgranular propagation for all models (Fig. 16) and the obtained FCGR curves almost coincide (Fig. 17, C4).

3.4 Discussion

Modelling the grain structure utilizing PD and evaluating the FCG behaviour and the FCGR in the C(T) Ti6Al4V alloy samples show the anisotropy in the FCG properties. The columnar grains in Section 3.3 are a good representation of the WAAM samples, where elongated β grains are growing parallel to the AM layer build direction [24,27]. The representation of the columnar grains in the H-C(T) sample, which are perpendicular to the crack propagation path (Fig. 15) showing the crack pathing repeatedly through the grains on its way and indicating that more resistance is occurring on the crack path (Fig. 17, C1). On the other hand, the V-C(T) samples show the sample's weaker response to the fatigue loading with the fast-propagating crack along the columnar grains because the pre-crack is parallel to the columnar grains. The same pattern of crack propagation in the different cuts of C(T) samples is noticed in the WAAM Ti6Al4V tests [14], where the H-C(T) sample has higher FCG resistance compared to V-C(T) sample due to the elongated β grains. On the other hand, since high pressure rolling of each AM layer can be applied to reduce the grain size and, as a result, to reduce the anisotropy in the material [27], the microstructure will no longer be columnar and β grains size is reduced to the one shown in Fig. 11, where the C(T) sample with the higher number of grains is indicating the rolled structure under higher rolling load. Due to the rolling procedures of WAAM, the effect of changed microstructure is noticed during FCG tests [56], where rolled samples show the FCGR close to the wrought Ti6Al4V and reduce scatter of FCGR properties in both H-C(T) and V-C(T) samples. Due to this, the PD grain model from Fig. 11 is the closest representation of the rolled WAAM samples, with the corresponding FCGR in Fig. 12 due to different sizes of the grains.

In addition, the samples produced by SLM without any heat treatment [21] show contrary results compared to WAAM samples. The crack propagates faster in H-C(T) samples, even if the structure has elongated β grains parallel to the layer build direction. The cause for such an outcome in FCGR could be the existence of very high residual stresses in the direction of crack propagation in H-C(T) sample. The applied heat-treatments show coarsening of the microstructure and a considerable reduction in residual stresses, which results in very close

FCGR for both layer orientations. The coarsening of microstructure shown in Fig. 11d and numerical simulations of the fatigue propagation indicate that the coarser grain in a sample is more resistant to FCG, as shown in Fig. 12d.

4 Influence of pores on the FCG

Another important effect to consider on FCGR is the existence of the pores in additively manufactured Ti6Al4V samples. Firstly, the porosities are initiated in the PD fatigue model, and the effect on the FCG behaviour is analysed. Secondly, the PD fatigue analysis is performed for the C(T) sample, which includes columnar grains and different levels of porosities. The porosities are initiates in the C(T) sample, shown in Fig. 7, with material properties and PD parameters described in Section 2.4. C(T) sample is under the load ratio of $\boldsymbol{R=0.1}$ with the cyclic load extreams of $\boldsymbol{F_y^{max}=7kN}$ and $\boldsymbol{F_y^{min}=0.7kN}$, applied to the sample by Eq. (18).

4.1 Modelling of pores in PD

Three major factors affect the fatigue life of the structure: microstructure, pores and residual stresses. Section 3 numerically showcased the effect of the material microstructure on the FCG, and the developed model of the columnar grains had a different fatigue performance with respect to the grain orientation. In this section, the interest is on the influence of the pores on the FCG behaviour.

The authors performed the study [43] on the effect of the pores on the fatigue crack nucleation in additively manufactured Ti6Al4V. The proposed numerical model for pores implementation in the PD fatigue nucleation showed good predictability of fatigue life of dog-bone samples under high cycle fatigue. Moreover, the model provided an estimation of critical pore sizes and their locations. In this respect, a similar PD fatigue model is applied to the FCG problem in the C(T) sample. The proposed model for pores initiation in the numerical model adopts Murakami's formulation [57], where the relation between the SIF and the porosity size is analysed with the porosity coefficient enforcement in the cumulative damage rule of fatigue PD model, shown in Eq. (8). Following that the Paris law can be expressed in terms of the cyclic bond strain ε, because ε is proportional to the SIF, a PD porosity model is implemented for both phases of fatigue crack nucleation and propagation stages, where the porosity coefficient added in Eq. (8) as:

$$\begin{cases} \dfrac{d\lambda(N)}{dN} = -kA_1(\varepsilon\chi)^{m_1} = -kA_1\left(\varepsilon\dfrac{\Delta K_p}{\Delta K_{th,p}}\right)^{m_1}, & \text{for Phase I} \\ \dfrac{d\lambda(N)}{dN} = -kA_2(\varepsilon\chi)^{m_2} = -kA_2\left(\varepsilon\dfrac{\Delta K_p}{\Delta K_{th,p}}\right)^{m_2}, & \text{for Phase II} \end{cases} \tag{23}$$

where parameter k is the strength coefficient introduced in Eq. (22) for grain boundaries and grain interior presentation. The enforced parameter χ represents the pores with different diameters of d_p in the relation between the SIF range, ΔK_p, and the SIF range limit. $\Delta K_{th,p}$, for specified pores. ΔK_p is evaluated by the Eq. (24), proposed by Murakami [57], where a new parameter $\sqrt{S}$ was adopted in El Haddad et al. [58] model to obtain the relationship between the SIF range and the porosity size. In the following model the spherical pore is treated as a crack with a size equal to the square root of the projected area of the pore, and the SIF range is estimated in the following form:

$$\Delta K_p = C\Delta\sigma\sqrt{\pi\sqrt{S}} \tag{24}$$

where $\Delta\sigma$ is the applied stress range, and the parameter C depends on the porosity defects location, where $C = 0.5$ is for internal pores, and $C = 0.65$ is for external pores [57].

The SIF range limit $\Delta K_{th,p}$ is evaluated by the proposed model in [59], where the smooth transition from the porosity defects to the long cracks is considered:

$$\sqrt{S_0} = \frac{1}{\pi}\left(\frac{\Delta K_{th,LC}}{\mathrm{C}\ \Delta\sigma_e}\right)^2 \tag{25}$$

$$\Delta K_{th,p} = \Delta K_{th,LC}\sqrt{\frac{\sqrt{S}}{\sqrt{S}+\sqrt{S_0}}} \tag{26}$$

$\Delta K_{th,LC}$ is the threshold SIF range for the long crack, and according to the tests in [18], $\Delta K_{th,LC} = 4.5\ MPa\sqrt{m}$ for the additively manufactured Ti6Al4V with the intrinsic fatigue limit of $\Delta\sigma_e = 540\ MPa$, when load ratio $R = 0.1$. The implemented porosity coefficient in the evolution law is increasing with the bigger pore diameter [43].

The analysis is performed for four different porosity levels of $P = 0.01, 0.04$, 0.08 and 0.2%. The indicated porosities are selected due to the sample observations in the published works [17,36,37]. The reference model is the C(T) sample from Section 2.4 with the porosity of $P = 0$.

To initiate the porosity in the PD model, Gamma distribution with the shape parameter of $r = 10$ is selected, as shown in Fig. 18. To satisfy the porosities chosen in a sample, the porosity ratio is evaluated in the following form:

$$P = \frac{V_p}{V_T} \tag{27}$$

where V_p is the volume of void-space and V_T is the bulk volume of material. In the PD model, V_p is the total volume of the selected pores with the identified diameters and V_T is the total volume of the C(T) sample. After the desired porosity is reached, the pores are randomly distributed over the sample. For example, with the porosity level of $P = 0.01\%$ in Fig. 18, the total number of $N_{p_{tot}} = 2324$ pores are randomly allocated in the sample with the maximum pore diameter of $d_p = 220\mu m$. The first row of Fig. 18 showing the Gamma distributions for each of the assigned porosities with the indication of the total number of the pores $N_{p_{tot}}$ within a sample. The second row shows the random porosity distributions corresponding to each of the porosity levels, where the samples with the $P > 0.01\%$ has more dense porosity distributions with the total number of pores of $N_{p_{tot}} > 4300$. Note that the size of pores in Fig. 18 are scaled only for visualisation purposes. Multiple crack interaction between neighbouring pores is taken into account, where the amplifying effect is considered [60], meaning that the interaction between the pores i and j is effecting the remaining life of the bond as:

$$\begin{cases} \dfrac{d\lambda_i(N)}{dN} = -kA_1\left(\varepsilon_i\chi_i\chi_j\right)^{m_1}, & \text{for Phase I} \\ \dfrac{d\lambda_i(N)}{dN} = -kA_2\left(\varepsilon_i\chi_i\chi_j\right)^{m_2}, & \text{for Phase II} \end{cases} \tag{28}$$

4.2 Results and discussion

The fatigue simulations are performed under the cyclic load amplitude of $F_a = 3.15\ kN$ with the load ratio of $R = 0.1$, and the material properties are the same as stated in Section 2.4 by omitting the influence of material microstructure ($k_{GI} = 1, k_{GB} = 1$). In all simulated cases, crack follows the path with higher density of pores and deflects towards the pores with a bigger diameter, as shown in Fig. 19. Only for the sample with the lowest porosity of $P = 0.01\%$ the crack growth is straight with a slight deflection at the end of its path. The small effect on crack propagation is noticed due to the pores' small porosities and low densities in front of the crack tip. The second row in Fig. 19 shows the pores that the crack is propagating through, where only 20 pores with the mean pore diameter of $d_p^{mean} = 77\mu m$ are noticed in the sample with $P = 0.01\%$. On the other hand, the samples with the porosities of $P = 0.04$, 0.08 and 0.2% have higher clusters of the pores on the crack path with the number of pores of 26, 35 and 37, and mean pore diameter of $d_p^{mean} = 86, 121$ and $168\ \mu m$, respectively. The samples with the higher porosity levels are weakening the sample's integrity and have a higher effect not only on the FCG behaviour but also on the FCGR. The $da/dN - \Delta K$ curves in Fig. 20 for C(T) sample with different porosity levels show the reduction of the fatigue strength due to the dense presence of the pores. Only the areas with pores of $d_p < 50\mu m$ or where the distance between the pores is more then $0.3 \times 10^{-3}\ m$, the FCGR are very close to the wrought Ti6Al4V ($P = 0$) and the effect of the pores on the FCGR is minimal, as shown in Fig. 20 for $P = 0.01\%$.

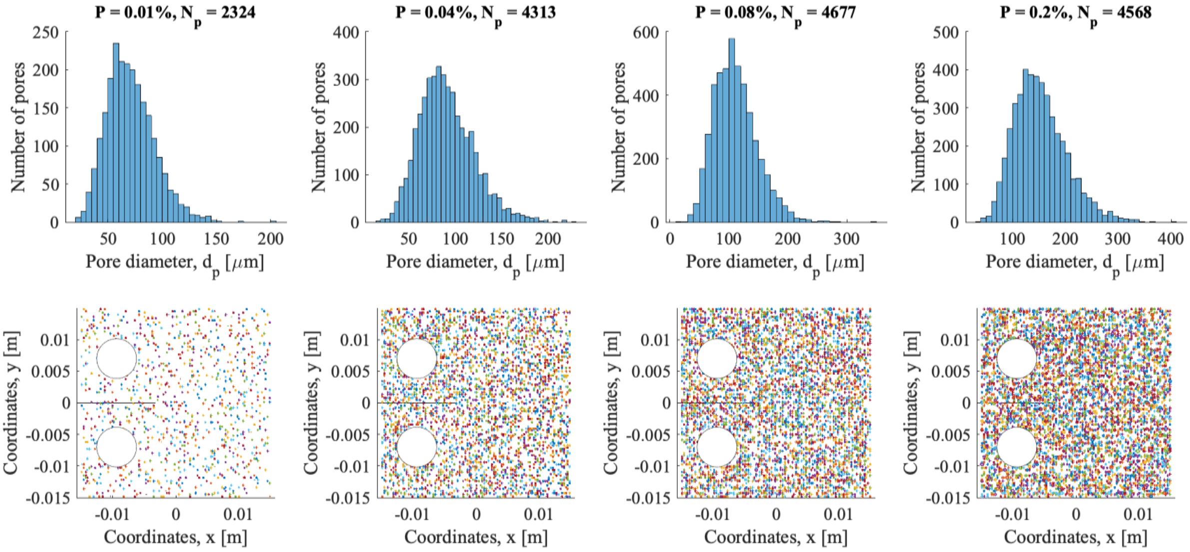

Fig. 18 Gamma distribution of the pores with porosities of $P = 0.01, 0.04,\ 0.08$ and 0.2%, and its corresponding distributions in the C(T) sample.

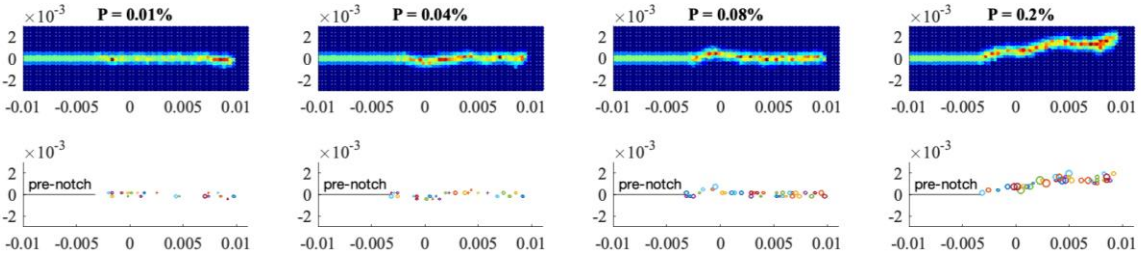

Fig. 19 Crack propagation plots and pore distributions in front of propagating crack in C(T) sample with different porosity levels.

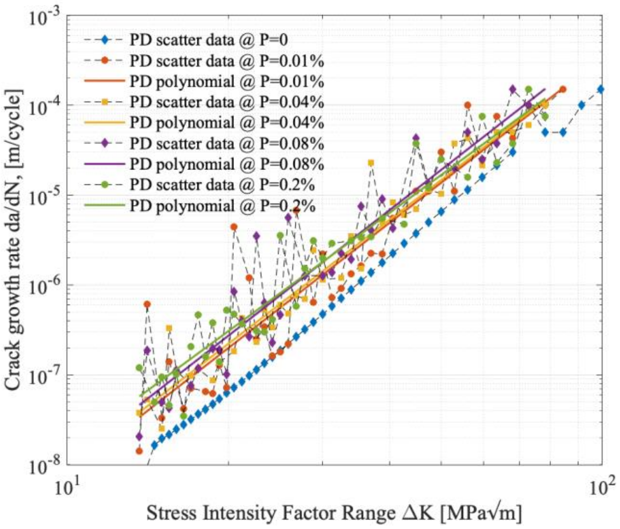

Fig. 20 Crack growth curves comparison for C(T) samples with different porosity.

From the presented numerical study, the effect of the porosities on the FCGR is evident with the low impact of the pores on FCG behaviour only in the samples with low porosity densities and small sizes of pores. This could be the reason why the test studies [21] showed a minor impact of the pores of the diameter of $d_p \leq 50\mu m$ on FCGR. Moreover, the study [15] of EBM Ti6Al4V samples showed non-uniform defect distributions in the AM part with different fatigue performances of the H-C(T) and V-C(T) samples. It was indicated that the core part of the built mainly was defect-free, and the highest concentration of the pores was closer to the built edges [15]. Therefore, it was concluded that the porosities did not have a significant contribution to FCG properties. Instead, the review in [38] had the contrary outcome with a definitive effect of the pores on the fatigue performance where it is stated that FCG behaviour is dependent not only on microstructure but also on process-induced defects, with the effect on the FCGR. With this respect, it is important to analyse the fatigue response of the C(T) specimen by considering the microstructure and process-induced defects, like pores. However, the sample's pore distribution can be regarded as uniform within the sample in the current studies, just with the small variations of pore concentrations. Therefore, the following simplification is made to analyse the worst-case scenario of the AM sample with high levels of porosities within all the sample structures and evaluate the effects of the pores on FCGR.

The PD fatigue model includes the two types of C(T) samples, shown in Fig. 1, with the granularity of C1 ($k_{GI} = 1, k_{GB} = 5$), described more in details in Section 3, and three levels of porosity $P = 0.01,\ 0.04$ and 0.08%. As shown, in Fig. 21 and Fig. 22, the H-C(T) samples has the long grains allocated perpendicular to the pre-notch; on the other hand, sample V-C(T) has the grain distribution parallel to the pre-notch. The long grains are presented in a grey pattern. The performed PD simulations for all porosity levels have shown transgranular crack propagation for H-C(T) and intergranular crack propagation for V-C(T) samples. In all the cases for H-C(T) samples, crack deflects toward the weakest areas with the higher densities of the pores but still propagates through the grains (Fig. 21). Evaluating the FCGR, the porosities have an apparent effect on the fatigue performance, wherein both types of samples, H-C(T) and V-C(T), the higher levels of porosities initiate the faster crack propagation resulting in the worth FCGR, shown in Fig. 23. Moreover, comparing the fatigue performance of H-C(T) and V-C(T) samples in Fig. 24 shows that H-C(T) samples are still more resistant to the FCG.

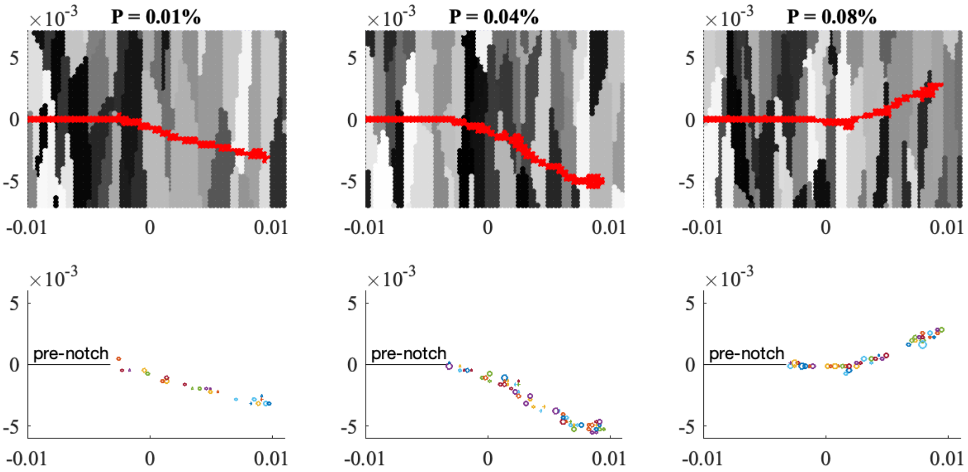

Fig. 21 Crack propagation plots and pore distributions in front of propagating crack in H-C(T) samples with different porosity levels of P.

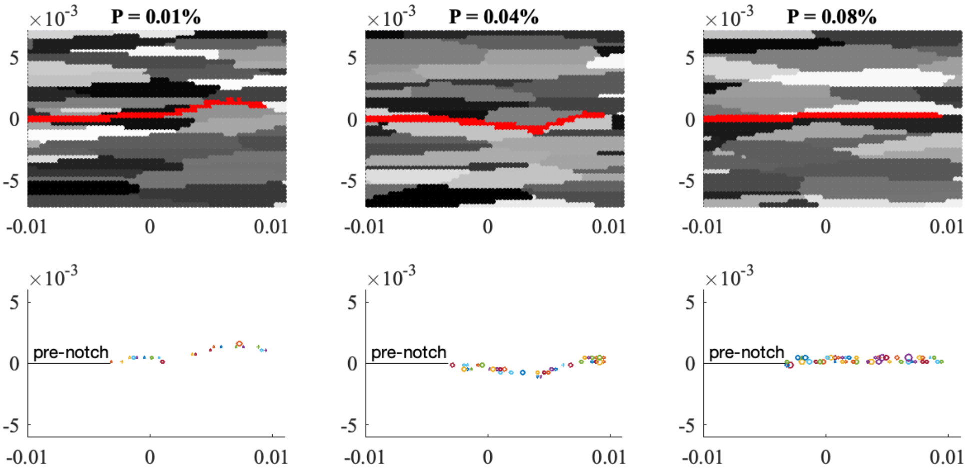

Fig. 22 Crack propagation plots and pore distributions in front of propagating crack in V-C(T) samples with different porosity levels of P.

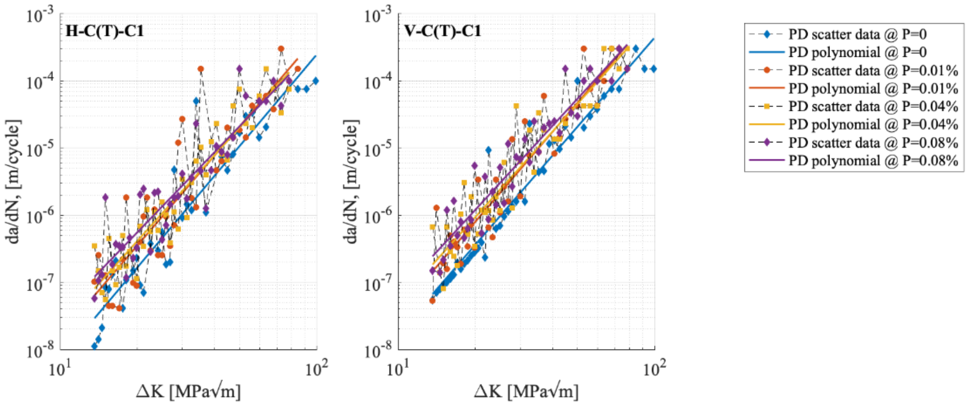

Fig. 23 Crack growth curves comparison between samples with different porosity levels of P and granularity of H-C(T) and V-C(T) samples.

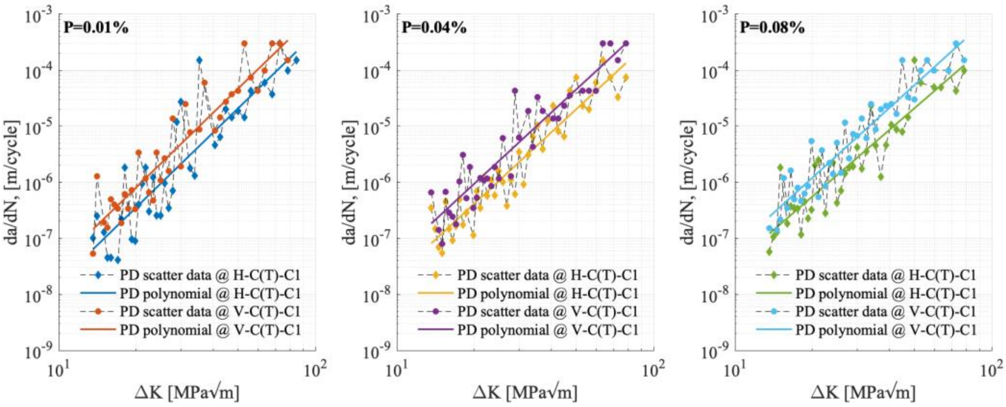

Fig. 24 Crack growth curves comparison between H-C(T) and V-C(T) samples with porosity of $P = 0.01$, 0.04 and 0.08%.

The PD study showed good assessment and indication of the porosity effects on the FCG even if the model is treated as elastic and the plastic deformations are neglected. All the pores are treated as spherical, and the cavities in the samples are evaluated using the pore diameter. The following assumption is made based on the test observations [9,19], where the most common process-induced defects are spherical pores. Thus, the PD FCG model accurately captures the small changes in the material structure and the effect of the small defects on the FCGR and FCG behaviour due to the pore existence. The initiation of granularity and porosity in the numerical model indicated the influence of both factors on fatigue performance. Firstly, it is showcased by means of numerical modelling the importance of porosity reduction in the samples, as even the low porosity levels of $P = 0.01\%$ with the distribution all over the sample have a noticeable impact on FCGR. Secondly, the numerical investigation on the columnar grains in the structure showed the anisotropy in the fatigue properties due to the development of a long-grained structure during the AM process.

5 Conclusion

This study investigated the influence of microstructure and porosity on the FCGR of additively manufactured Ti6Al4V material. These effects were evaluated based on the types of microstructure and porosity levels available in the literature. The employment of PD theory in fatigue problems showed the PD fatigue model's capability to capture the FCG behaviour, and the results of the validated model are in line with test data. The following conclusions can be derived from the conducted study:

- The crack propagation behaviour is directly dependent on the material microstructure, and coarse-grained microstructure has higher FCG resistance. Moreover, the columnar type of microstructure developed during AM brings the anisotropy into fatigue properties. The samples with the elongated $\boldsymbol{\beta}$ grains located parallel to the crack propagation path have a weaker response with the fast-propagating crack along the columnar grains.

- The pores in the presented samples impact the FCG behaviour, where the crack moves through the areas with a higher density of the pores with bigger diameters. The porosities weaken structural integrity with faster FCGR for the samples with higher levels of porosities.
- The model with implemented porosities and columnar microstructure showed the effect of both factors on the FCGR. The cut of the samples with different columnar grains orientation contributes to the anisotropy of FCG performance. Even low levels of porosities ($\mathbf{P} = \mathbf{0.01}\%$) are increasing the FCGR.

References

[1] W.E. Frazier, Metal additive manufacturing: A review, J. Mater. Eng. Perform. 23 (2014) 1917–1928. https://doi.org/10.1007/s11665-014-0958-z.

[2] L.E. Murr, E. Martinez, K.N. Amato, S.M. Gaytan, J. Hernandez, D.A. Ramirez, P.W. Shindo, F. Medina, R.B. Wicker, Fabrication of metal and alloy components by additive manufacturing: Examples of 3D materials science, J. Mater. Res. Technol. 1 (2012) 42–54. https://doi.org/10.1016/S2238-7854(12)70009-1.

[3] J.-P. Kruth, M.C. Leu, T. Nakagawa, Progress in Additive Manufacturing and Rapid Prototyping, CIRP Ann. 47 (1998) 525–540. https://doi.org/10.1016/s0007-8506(07)63240-5.

[4] Y. Zhai, D.A. Lados, J.L. Lagoy, Additive Manufacturing: Making imagination the major Limitation, Jom. 66 (2014) 808–816. https://doi.org/10.1007/s11837-014-0886-2.

[5] T.D. Ngo, A. Kashani, G. Imbalzano, K.T.Q. Nguyen, D. Hui, Additive manufacturing (3D printing): A review of materials, methods, applications and challenges, Compos. Part B Eng. 143 (2018) 172–196. https://doi.org/10.1016/j.compositesb.2018.02.012.

[6] J.D. Strickland, Applications of Additive Manufacturing in the marine industry, PRADS 2016 - Proc. 13th Int. Symp. Pract. Des. Ships Other Float. Struct. (2016). https://doi.org/10.13140/RG.2.2.29930.31685.

[7] S. Chandrasekaran, S. Hari, M. Amirthalingam, Wire arc additive manufacturing of functionally graded material for marine risers, Mater. Sci. Eng. A. 792 (2020) 139530. https://doi.org/10.1016/j.msea.2020.139530.

[8] D. Bourell, J.P. Kruth, M. Leu, G. Levy, D. Rosen, A.M. Beese, A. Clare, Materials for additive manufacturing, CIRP Ann. - Manuf. Technol. 66 (2017) 659–681. https://doi.org/10.1016/j.cirp.2017.05.009.

[9] T. DebRoy, H.L. Wei, J.S. Zuback, T. Mukherjee, J.W. Elmer, J.O. Milewski, A.M. Beese, A. Wilson-Heid, A. De, W. Zhang, Additive manufacturing of metallic components – Process, structure and properties, Prog. Mater. Sci. 92 (2018) 112–224. https://doi.org/10.1016/j.pmatsci.2017.10.001.

[10] D. Herzog, V. Seyda, E. Wycisk, C. Emmelmann, Additive manufacturing of metals, Acta Mater. 117 (2016) 371–392. https://doi.org/10.1016/j.actamat.2016.07.019.

[11] B. Dutta, F.H. (Sam). Froes, The Additive Manufacturing (AM) of titanium alloys, Elsevier Inc., 2017. https://doi.org/10.1016/j.mprp.2016.12.062.

[12] D. Greitemeier, F. Palm, F. Syassen, T. Melz, Fatigue performance of additive manufactured TiAl6V4 using electron and laser beam melting, Int. J. Fatigue. 94 (2017) 211–217. https://doi.org/10.1016/j.ijfatigue.2016.05.001.

[13] A.B. Spierings, T.L. Starr, K. Wegener, Fatigue performance of additive manufactured metallic parts,

Rapid Prototyp. J. 19 (2013) 88–94. https://doi.org/10.1108/13552541311302932.

[14] Y. Xie, M. Gao, F. Wang, C. Zhang, K. Hao, H. Wang, X. Zeng, Anisotropy of fatigue crack growth in wire arc additive manufactured Ti-6Al-4V, Mater. Sci. Eng. A. 709 (2018) 265–269. https://doi.org/10.1016/j.msea.2017.10.064.

[15] M. Seifi, A. Salem, D. Satko, J. Shaffer, J.J. Lewandowski, Defect distribution and microstructure heterogeneity effects on fracture resistance and fatigue behavior of EBM Ti–6Al–4V, Int. J. Fatigue. 94 (2017) 263–287. https://doi.org/10.1016/j.ijfatigue.2016.06.001.

[16] Y. Kok, X.P. Tan, P. Wang, M.L.S. Nai, N.H. Loh, E. Liu, S.B. Tor, Anisotropy and heterogeneity of microstructure and mechanical properties in metal additive manufacturing: A critical review, Mater. Des. 139 (2018) 565–586. https://doi.org/10.1016/j.matdes.2017.11.021.

[17] L. Thijs, F. Verhaeghe, T. Craeghs, J. Van Humbeeck, J.P. Kruth, A study of the microstructural evolution during selective laser melting of Ti-6Al-4V, Acta Mater. 58 (2010) 3303–3312. https://doi.org/10.1016/j.actamat.2010.02.004.

[18] R. Biswal, X. Zhang, A.K. Syed, M. Awd, J. Ding, F. Walther, S. Williams, Criticality of porosity defects on the fatigue performance of wire + arc additive manufactured titanium alloy, Int. J. Fatigue. 122 (2019) 208–217. https://doi.org/10.1016/j.ijfatigue.2019.01.017.

[19] T. Mukherjee, J.S. Zuback, A. De, T. Debroy, Printability of alloys for additive manufacturing, Sci. Rep. 6 (2016) 19717. https://doi.org/10.1038/srep19717.

[20] M.R. Khosravani, F. Berto, M.R. Ayatollahi, T. Reinicke, Fracture behavior of additively manufactured components: A review, Theor. Appl. Fract. Mech. 109 (2020) 102763. https://doi.org/10.1016/j.tafmec.2020.102763.

[21] S. Leuders, M. Thöne, A. Riemer, T. Niendorf, T. Tröster, H.A. Richard, H.J. Maier, On the mechanical behaviour of titanium alloy TiAl6V4 manufactured by selective laser melting: Fatigue resistance and crack growth performance, Int. J. Fatigue. 48 (2013) 300–307. https://doi.org/10.1016/j.ijfatigue.2012.11.011.

[22] R.K. Nalla, B.L. Boyce, J.P. Campbell, J.O. Peters, R.O. Ritchie, Influence of Microstructure on High-Cycle Fatigue of Ti-6Al-4V: Bimodal vs. Lamellar Structures, Metall. Mater. Trans. A Phys. Metall. Mater. Sci. 33A (2002). https://doi.org/10.13140/RG.2.1.3668.1201.

[23] R. Pederson, Microstructure and Phase Transformation of Ti-6Al-4V, (2002) 27–30.

[24] P. Åkerfeldt, R. Pederson, M.L. Antti, A fractographic study exploring the relationship between the low cycle fatigue and metallurgical properties of laser metal wire deposited Ti-6Al-4V, Int. J. Fatigue. 87 (2016) 245–256. https://doi.org/10.1016/j.ijfatigue.2016.02.011.

[25] B. Baufeld, E. Brandl, O. Van Der Biest, Wire based additive layer manufacturing: Comparison of microstructure and mechanical properties of Ti-6Al-4V components fabricated by laser-beam deposition and shaped metal deposition, J. Mater. Process. Technol. 211 (2011) 1146–1158. https://doi.org/10.1016/j.jmatprotec.2011.01.018.

[26] E. Brandl, F. Palm, V. Michailov, B. Viehweger, C. Leyens, Mechanical properties of additive manufactured titanium (Ti-6Al-4V) blocks deposited by a solid-state laser and wire, Mater. Des. 32 (2011) 4665–4675. https://doi.org/10.1016/j.matdes.2011.06.062.

[27] F. Martina, P.A. Colegrove, S.W. Williams, J. Meyer, Microstructure of Interpass Rolled Wire + Arc Additive Manufacturing Ti-6Al-4V Components, Metall. Mater. Trans. A Phys. Metall. Mater. Sci. 46 (2015) 6103–6118. https://doi.org/10.1007/s11661-015-3172-1.

[28] S. Liu, Y.C. Shin, Additive manufacturing of Ti6Al4V alloy: A review, Mater. Des. 164 (2019) 107552.

https://doi.org/10.1016/j.matdes.2018.107552.

[29] M. Simonelli, Y.Y. Tse, C. Tuck, Effect of the build orientation on the mechanical properties and fracture modes of SLM Ti-6Al-4V, Mater. Sci. Eng. A. 616 (2014) 1–11. https://doi.org/10.1016/j.msea.2014.07.086.

[30] T. Morita, C. Tsuda, H. Sakai, N. Higuchi, Fundamental properties of Ti-6Al-4V alloy produced by selective laser melting method, Mater. Trans. 58 (2017) 1397–1403. https://doi.org/10.2320/matertrans.M2017103.

[31] B. Van Hooreweder, D. Moens, R. Boonen, J.P. Kruth, P. Sas, Analysis of fracture toughness and crack propagation of Ti6Al4V produced by selective laser melting, Adv. Eng. Mater. 14 (2012) 92–97. https://doi.org/10.1002/adem.201100233.

[32] A. Riemer, S. Leuders, M. Thöne, H.A. Richard, T. Tröster, T. Niendorf, On the fatigue crack growth behavior in 316L stainless steel manufactured by selective laser melting, Eng. Fract. Mech. 120 (2014) 15–25. https://doi.org/10.1016/j.engfracmech.2014.03.008.

[33] E. Wycisk, S. Siddique, D. Herzog, F. Walther, C. Emmelmann, Fatigue performance of laser additive manufactured Ti–6Al–4V in very high cycle fatigue regime up to 10 9 cycles, Front. Mater. 2 (2015) 2–9. https://doi.org/10.3389/fmats.2015.00072.

[34] R. Biswal, A.K. Syed, X. Zhang, Assessment of the effect of isolated porosity defects on the fatigue performance of additive manufactured titanium alloy, Addit. Manuf. 23 (2018) 433–442. https://doi.org/10.1016/j.addma.2018.08.024.

[35] J. Günther, D. Krewerth, T. Lippmann, S. Leuders, T. Tröster, A. Weidner, H. Biermann, T. Niendorf, Fatigue life of additively manufactured Ti–6Al–4V in the very high cycle fatigue regime, Int. J. Fatigue. 94 (2017) 236–245. https://doi.org/10.1016/j.ijfatigue.2016.05.018.

[36] S. Tammas-Williams, P.J. Withers, I. Todd, P.B. Prangnell, The Influence of Porosity on Fatigue Crack Initiation in Additively Manufactured Titanium Components, Sci. Rep. 7 (2017) 1–13. https://doi.org/10.1038/s41598-017-06504-5.

[37] G. Kasperovich, J. Hausmann, Improvement of fatigue resistance and ductility of TiAl6V4 processed by selective laser melting, J. Mater. Process. Technol. 220 (2015) 202–214. https://doi.org/10.1016/j.jmatprotec.2015.01.025.

[38] J.J. Lewandowski, M. Seifi, Metal Additive Manufacturing: A Review of Mechanical Properties, Annu. Rev. Mater. Res. 46 (2016) 151–186. https://doi.org/10.1146/annurev-matsci-070115-032024.

[39] S.A. Silling, Reformulation of elasticity theory for discontinuities and long-range forces, J. Mech. Phys. Solids. 48 (2000) 175–209. https://doi.org/10.1016/S0022-5096(99)00029-0.

[40] E. Oterkus, I. Guven, E. Madenci, Fatigue failure model with peridynamic theory, in: 2010 12th IEEE Intersoc. Conf. Therm. Thermomechanical Phenom. Electron. Syst., IEEE, 2010. https://doi.org/10.1109/itherm.2010.5501273.

[41] S. Silling, A. Askari, Peridynamic model for fatigue cracks, 2014. http://docs.lib.purdue.edu/ses2014/mss/cfm/22/%0Ahttps://www.osti.gov/scitech/biblio/1160289-peridynamic-model-fatigue-cracking.

[42] G. Zhang, Q. Le, A. Loghin, A. Subramaniyan, F. Bobaru, Validation of a peridynamic model for fatigue cracking, Eng. Fract. Mech. 162 (2016) 76–94. https://doi.org/10.1016/j.engfracmech.2016.05.008.

[43] O. Karpenko, S. Oterkus, E. Oterkus, Peridynamic Investigation of the Effect of Porosity on Fatigue Nucleation for Additively Manufactured Titanium Alloy Ti6Al4V, Theor. Appl. Fract. Mech. (2021) 102925. https://doi.org/10.1016/j.tafmec.2021.102925.

[44] B. Kilic, E. Madenci, An adaptive dynamic relaxation method for quasi-static simulations using the peridynamic theory, Theor. Appl. Fract. Mech. 53 (2010) 194–204. https://doi.org/10.1016/j.tafmec.2010.08.001.

[45] E. Madenci, E. Oterkus, Peridynamic Theory and Its Applications, Springer New York Heidelberg Dordrecht London, 2014. https://doi.org/DOI 10.1007/978-1-4614-8465-3.

[46] S.A. Silling, E. Askari, A meshfree method based on the peridynamic model of solid mechanics, Comput. Struct. 83 (2005) 1526–1535. https://doi.org/10.1016/j.compstruc.2004.11.026.

[47] S.A. Silling, F. Bobaru, Peridynamic modeling of membranes and fibers, Int. J. Non. Linear. Mech. 40 (2005) 395–409. https://doi.org/10.1016/j.ijnonlinmec.2004.08.004.

[48] J. Zhang, X. Wang, S. Paddea, X. Zhang, Fatigue crack propagation behaviour in wire+arc additive manufactured Ti-6Al-4V: Effects of microstructure and residual stress, Mater. Des. 90 (2016) 551–561. https://doi.org/10.1016/j.matdes.2015.10.141.

[49] C. Dyyaroglu, Peridynamics and its applications in marine structures, University of Strathclyde, 2016.

[50] H.A. Van der Vorst, Bi-CGSTAB: A Fast and Smoothly Converging Variant of Bi-CG for the Solution of Nonsymmetric Linear Systems, SIAM J. Sci. Stat. Comput. 13 (1992) 631–644. https://doi.org/https://doi.org/10.1137/0913035.

[51] X. Liu, C. Sun, Y. Hong, Effects of stress ratio on high-cycle and very-high-cycle fatigue behavior of a Ti-6Al-4V alloy, Mater. Sci. Eng. A. 622 (2015) 228–235. https://doi.org/10.1016/j.msea.2014.09.115.

[52] ASTM E647−13, Standard Test Method for Measurement of Fatigue Crack Growth Rates, Am. Soc. Test. Mater. 03 (2014) 1–50. https://doi.org/10.1520/E0647-13A.2.

[53] E. Askari, F. Bobaru, R.B. Lehoucq, M.L. Parks, S.A. Silling, O. Weckner, Peridynamics for multiscale materials modeling, J. Phys. Conf. Ser. 125 (2008). https://doi.org/10.1088/1742-6596/125/1/012078.

[54] O.M. Ivasishin, P.E. Markovsky, Enhancing the mechanical properties of titanium alloys with rapid heat treatment, Jom. 48 (1996) 48–52. https://doi.org/10.1007/BF03222998.

[55] S. Jafarzadeh, Z. Chen, F. Bobaru, Peridynamic Modeling of Intergranular Corrosion Damage, J. Electrochem. Soc. 165 (2018) C362–C374. https://doi.org/10.1149/2.0821807jes.

[56] Q. Xudong, Effect of rolling on fatigue crack growth rate of wire and arc additive manufacture (WAAM) processed titanium, 2013.

[57] Y. Murakami, Effects of small defects and nonmetallic inclusions on the fatigue strength of metals, Mech. Corros. Prop. Ser. A, Key Eng. Mater. 51–52 (1991) 37–42. https://doi.org/10.4028/www.scientific.net/kem.51-52.37.

[58] M.H. El Haddad, T.H. Topper, K.. Smith, Prediction of non propagating cracks, Eng. Fract. Mech. 11 (1978) 573–584.

[59] S. Beretta, S. Romano, A comparison of fatigue strength sensitivity to defects for materials manufactured by AM or traditional processes, Int. J. Fatigue. 94 (2017) 178–191. https://doi.org/10.1016/j.ijfatigue.2016.06.020.

[60] O. Karpenko, S. Oterkus, E. Oterkus, Influence of Different Types of Small-Size Defects on Propagation of Macro-cracks in Brittle Materials, J. Peridynamics Nonlocal Model. 2 (2020) 289–316. https://doi.org/10.1007/s42102-020-00032-z.